



Contents lists available at ScienceDirect

Journal of Colloid and Interface Science

journal homepage: [www.elsevier.com/locate/jcis](http://www.elsevier.com/locate/jcis)

# Multifunctional magnetic Fe<sub>3</sub>O<sub>4</sub>/Cu<sub>2</sub>O-Ag nanocomposites with high sensitivity for SERS detection and efficient visible light-driven photocatalytic degradation of polycyclic aromatic hydrocarbons (PAHs)

Jie Huang<sup>a</sup>, Tianxiang Zhou<sup>a</sup>, Wenshi Zhao<sup>a,b,c</sup>, Sicheng Cui<sup>a</sup>, Rui Guo<sup>a</sup>, Dan Li<sup>a</sup>, Naveen Reddy Kadasala<sup>d</sup>, Donglai Han<sup>f</sup>, Yuhong Jiang<sup>a</sup>, Yang Liu<sup>a,e,\*</sup>, Huilian Liu<sup>a,\*</sup>

<sup>a</sup> Key Laboratory of Functional Materials Physics and Chemistry of the Ministry of Education, Jilin Normal University, Changchun 130103, PR China

<sup>b</sup> Changchun Institute of Optics, Fine Mechanics and Physics, Chinese Academy of Sciences, Changchun 130033, PR China

<sup>c</sup> University of Chinese Academy of Sciences, Beijing 100049, PR China

<sup>d</sup> Department of Chemistry, Towson University, Towson, MD 21252, United States

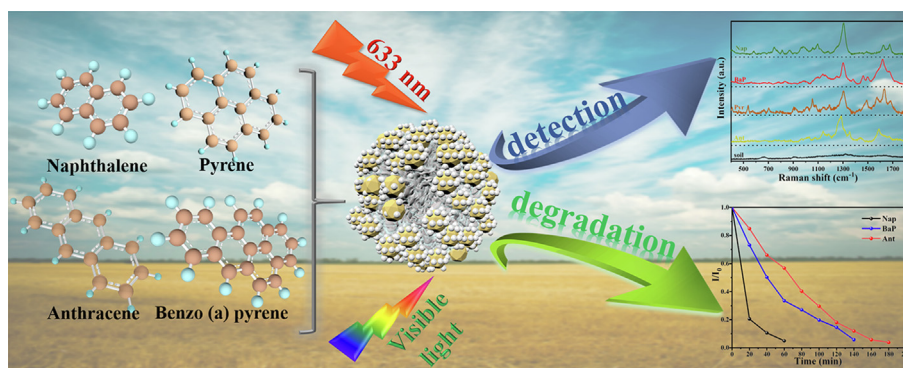
<sup>e</sup> Key Laboratory of Novel Materials for Sensor of Zhejiang Province, Hangzhou Dianzi University, Hangzhou 310012, PR China

<sup>f</sup> School of Materials Science and Engineering, Changchun University of Science and Technology, Changchun 130022, PR China

## HIGHLIGHTS

- Fe<sub>3</sub>O<sub>4</sub>/Cu<sub>2</sub>O-Ag nanocomposites (NCs) were designed and synthesized successfully.
- We realized integration of SERS detection and photocatalytic degradation for PAHs.
- Effect of Ag contents on SERS and catalytic activity of Fe<sub>3</sub>O<sub>4</sub>/Cu<sub>2</sub>O-Ag was studied.
- SERS detection limit of Fe<sub>3</sub>O<sub>4</sub>/Cu<sub>2</sub>O-Ag towards PAHs was as low as 10<sup>-9</sup> to 10<sup>-10</sup> M.
- Photocatalytic mechanism of PAHs degradation by Fe<sub>3</sub>O<sub>4</sub>/Cu<sub>2</sub>O-Ag was proposed.

## GRAPHICAL ABSTRACT



## ARTICLE INFO

### Article history:

Received 19 June 2022

Revised 19 July 2022

Accepted 6 August 2022

Available online 17 August 2022

### Keywords:

Magnetic

Fe<sub>3</sub>O<sub>4</sub>/Cu<sub>2</sub>O-Ag nanocomposites

Surface-enhanced Raman scattering

Photocatalytic degradation

Polycyclic aromatic hydrocarbons

## ABSTRACT

Polycyclic aromatic hydrocarbons (PAHs) with carcinogenic, teratogenic and mutagenic properties are persistent organic pollutants in the environment. Herein, the novel multifunctional Fe<sub>3</sub>O<sub>4</sub>/Cu<sub>2</sub>O-Ag nanocomposites (NCs) have been established for ultra-sensitive surface-enhanced Raman scattering (SERS) detection and visible light-driven photocatalytic degradation of PAHs. Fe<sub>3</sub>O<sub>4</sub>/Cu<sub>2</sub>O-Ag NCs with different amounts of Ag nanocrystals were synthesized, and the effect of Ag contents on SERS performance was studied by finite-difference time-domain (FDTD) algorithm. The synergistic interplay of electromagnetic and chemical enhancement was responsible for excellent SERS sensitivity of Fe<sub>3</sub>O<sub>4</sub>/Cu<sub>2</sub>O-Ag NCs. The limit of detection (LOD) of optimal SERS substrates (FCA-2 NCs) for Nap, BaP, Pyr and Ant was as low as 10<sup>-9</sup>, 10<sup>-9</sup>, 10<sup>-9</sup> and 10<sup>-10</sup> M, respectively. The SERS detection of PAHs in actual soil environment was also studied. Moreover, a simple SERS method was used to monitor the photocatalytic process of PAHs. The recovery and reuse of Fe<sub>3</sub>O<sub>4</sub>/Cu<sub>2</sub>O-Ag NCs were achieved through magnetic field, and the outstanding SERS and photocatalytic performance were still maintained even after eight cycles. This magnetic multifunctional NCs provide a unique idea for the integration of ultra-sensitive SERS detection

\* Corresponding authors.

E-mail addresses: [liuyang@jlnu.edu.cn](mailto:liuyang@jlnu.edu.cn) (Y. Liu), [lhl541@126.com](mailto:lhl541@126.com) (H. Liu).

and efficient photocatalytic degradation of PAHs, and thus will have more hopeful prospects in the field of environmental protection.

© 2022 Elsevier Inc. All rights reserved.

## 1. Introduction

Polycyclic aromatic hydrocarbons (PAHs) are referred to persistent organic pollutants with two or more benzene rings [1–3]. The sources of PAHs include natural sources such as biosynthetic processes of terrestrial and aquatic plants, volcanic ejecta, forest fire and prairie fire, and anthropogenic sources like incomplete combustion of hydrocarbons, wood and fossil fuels, which results in an extremely wide distribution of PAHs in a variety of environments [4,5]. In particular, owing to the high hydrophobic nature of PAHs, the solubility of PAHs is very low in water, which inevitably leads to their strong adsorption in environment, especially in soil, and thus aggravates their accumulation and enrichment in soils [6–8]. However, it is proven that PAHs and their derivatives have teratogenic, mutagenic and carcinogenic risks [9,10]. Even traces of PAHs pose serious threats to human health and cause a variety of diseases, including skin inflammation, kidney and liver damage, metabolic disorders and heart malformations [11,12]. So, it is imperative to design and develop a novel method to realize highly sensitive detection of PAHs in soils and efficient removal of PAHs from soils.

Several advanced technologies have been employed to identify PAHs in soil samples, and the most commonly used methods for sensitive detection of PAHs mainly include gas chromatography-mass spectrometry (GC-MS) [13] and high-performance liquid chromatography (HPLC) [14]. Although these conventional methods possess their own advantages, they are often complex, time-consuming, laborious and costly. Surface-enhanced Raman scattering (SERS) technology, as a simple, fast, cost-effective and efficient technique, is considered to be a promising analytical method for ultra-sensitive analysis of environmental pollutants. Recently, substantial research interests on trace detection of PAHs by SERS are continuously emerging [15–17]. In view of localized surface plasmon resonance (LSPR) characteristics of noble metal plasmonic materials [18], Ag and Au are the most prevalent SERS active substrates for PAHs detection [19,20], given that a considerable electromagnetic field enhancement can be generated at the surfaces of noble metals [21]. But from the perspective of SERS enhancement mechanism, the enhancement of SERS signals depends on two factors – electromagnetic enhancement (EM) as well as chemical enhancement (CE) [22]. Although EM is recognized as a key contribution to SERS enhancement, we should not overlook the role of CE. Combination of semiconductor and noble metal is an effective way to generate CE, which can promote charge transfer (CT) between semiconductor and noble metal and thereby, accelerate CT from SERS substrates to analyte molecules [23]. Moreover, high absorption capacity of SERS substrates to target molecules is another crucial factor to achieve a high SERS enhancement [24]. Generally, PAHs molecules show a quite weak adhesion to metallic surfaces, which is very unfavorable for the SERS detection of PAHs [25,26]. To deal with this issue, much work has focused on the surface functionalization of noble metals with various functional groups [27]. However, these surface functional groups generally produce interfering SERS signals, which will undoubtedly lower the SERS detection sensitivity. Fortunately, apart from the fact that the synergistic effect of EM and CE can enhance the SERS signals of PAHs molecules, the combination of semiconductor and noble metal can facilitate the adsorption of hydrophobic PAHs on SERS substrates [28]. But it is noteworthy that the integration of sensi-

tive detection and efficient removal of PAHs has always been a complicated and challenging research topic so far.

The efficient removal of PAHs from contaminated soils is another challenging task. At present, the effective means for removing PAHs mainly include ozone treatment [29], magnetic solid-phase extraction (MSPE) [30], adsorption [31], bioremediation [32] and photodegradation [33]. Among these various strategies for PAHs removal, photocatalytic degradation technology has attracted extensive concern because of its facile operation, low energy consumption and environmental friendliness. Conventional semiconductor photocatalysts such as ZnO and TiO<sub>2</sub> with a wide band gap have been used for the catalytic degradation of PAHs [34,35]. However, these photocatalysts can only be excited by ultraviolet (UV) irradiation, accounting for a small percentage of solar energy (only 4 %), which cannot make full use of solar energy [36]. By comparison, Cu<sub>2</sub>O, a kind of narrow band gap semiconductor, can be easily excited by visible light occupying about 43 % of solar energy [37]. Nonetheless, photogenerated electron-hole pairs in Cu<sub>2</sub>O tend to recombine, which restricts the photocatalytic efficiency of Cu<sub>2</sub>O [38]. Aiming at boosting the separation and transfer of photogenerated electron-hole pairs and hence enhancing the photocatalytic efficiency of Cu<sub>2</sub>O, the construction of semiconductor-plasmonic metal heterostructures has been proven to be an effective way owing to the appearance of Schottky barrier at the semiconductors/plasmonic metals interfaces [39]. Furthermore, the plasmonic metals can transfer the absorbed light energy to Cu<sub>2</sub>O and subsequently prompt Cu<sub>2</sub>O to generate more photogenerated electron-hole pairs [40,41]. Therefore, semiconductor-/plasmonic metal nanocomposites (NCs) not only can serve as SERS sensors for PAHs, but also can achieve the photocatalytic degradation of PAHs. As far as we know, however, little note has been taken on the integration of ultra-sensitive detection and efficient degradation of PAHs so far.

Recycling of NCs is a prerequisite for sustainable environmental monitoring and remediation. Most frequently used methods for separation of NCs involve centrifugation, filtration and sedimentation, but the procedures of these separation technologies are tedious, time-consuming and render loss of functional properties [42]. Magnetic separation technique possesses advantages of convenient operation and time saving, and superparamagnetic Fe<sub>3</sub>O<sub>4</sub> nanocrystals with large specific surface area and high saturation magnetization have been optimal choice for magnetic supports [43]. In order to adhere semiconductor/plasmonic metal to surfaces of Fe<sub>3</sub>O<sub>4</sub> nanocrystals, modification of Fe<sub>3</sub>O<sub>4</sub> nanocrystals with polymer (e.g. resorcinol-formaldehyde (RF) resins) is indispensable [44]. Uniform RF resin shells are lightly molded on the surfaces of Fe<sub>3</sub>O<sub>4</sub> nanocrystals because of the strong interactions between metal ions as well as phenolic hydroxyl groups [45]. In addition, RF resin shells protect Fe<sub>3</sub>O<sub>4</sub> nanocrystals from oxidation, aggregation, and shield the interferences of Raman signals originated from Fe<sub>3</sub>O<sub>4</sub> nanocrystals.

Inspired by the above ideas, we developed a multifunctional Fe<sub>3</sub>O<sub>4</sub>/Cu<sub>2</sub>O-Ag nanocomposite, which could act as an ultra-sensitive SERS sensor and possess effective photocatalyst activity driven by visible light. 4-mercaptobenzoic acid (4-MBA) was chosen as reporter molecule to discuss the effect of Ag contents on SERS activity. The “hot spot” distribution was simulated using finite-difference time-domain (FDTD) algorithm, and corresponding SERS enhancement mechanism was analyzed. Fe<sub>3</sub>O<sub>4</sub>/Cu<sub>2</sub>O-Ag

NCs were served as SERS sensor to realize SERS detection of PAHs in soils. In addition, photocatalytic performance of  $\text{Fe}_3\text{O}_4/\text{Cu}_2\text{O}$ -Ag NCs for degradation of PAHs under visible light was studied, and photocatalytic mechanism was also proposed. It was proved that the addition of Ag nanocrystals led to formation of Schottky barriers at interfaces between Ag and  $\text{Cu}_2\text{O}$ , which improved the photocatalytic activity of  $\text{Fe}_3\text{O}_4/\text{Cu}_2\text{O}$ -Ag NCs. Meanwhile, due to the existence of  $\text{Fe}_3\text{O}_4$  nanocrystals,  $\text{Fe}_3\text{O}_4/\text{Cu}_2\text{O}$ -Ag NCs could be conveniently recovered by a magnet and the repeatability of  $\text{Fe}_3\text{O}_4/\text{Cu}_2\text{O}$ -Ag NCs for SERS detection and photocatalytic degradation of PAHs could be achieved. This work not only enlarges research about SERS and photocatalytic mechanism of multifunctional sensors, but provides a bright future for the tailored design of recyclable and efficient hybrid sensor for detection and degradation of PAHs at the mass production level.

## 2. Experimental section

### 2.1. Materials and characterization

The information about materials and characterization are recorded in [Supplementary Materials](#).

### 2.2. Synthesis of $\text{Fe}_3\text{O}_4/\text{Cu}_2\text{O}$ and $\text{Fe}_3\text{O}_4/\text{Cu}_2\text{O}$ -Ag NCs

As shown in [Scheme 1a](#) and [1b](#), the flower ball-like  $\text{Fe}_3\text{O}_4$  nanocrystals were prepared by solvothermal method. And  $\text{Fe}_3\text{O}_4@\text{RF}$  nanocrystals were prepared on the basis of the flower ball-like  $\text{Fe}_3\text{O}_4$  nanocrystals. The preparation process is listed in [Supplementary Materials](#) in detail.

As presented in [Scheme 1c](#), 45 mg of  $\text{Fe}_3\text{O}_4@\text{RF}$  NCs was dispersed in deionized water. Next, 5 mL of  $\text{CuCl}_2$  (0.11 M) was dripped under sonication. Subsequently, 1.8 mL of NaOH (1.0 M) as well as 12 mL of  $\text{NH}_2\text{OH}\cdot\text{HCl}$  (0.1 M) were poured and stirred

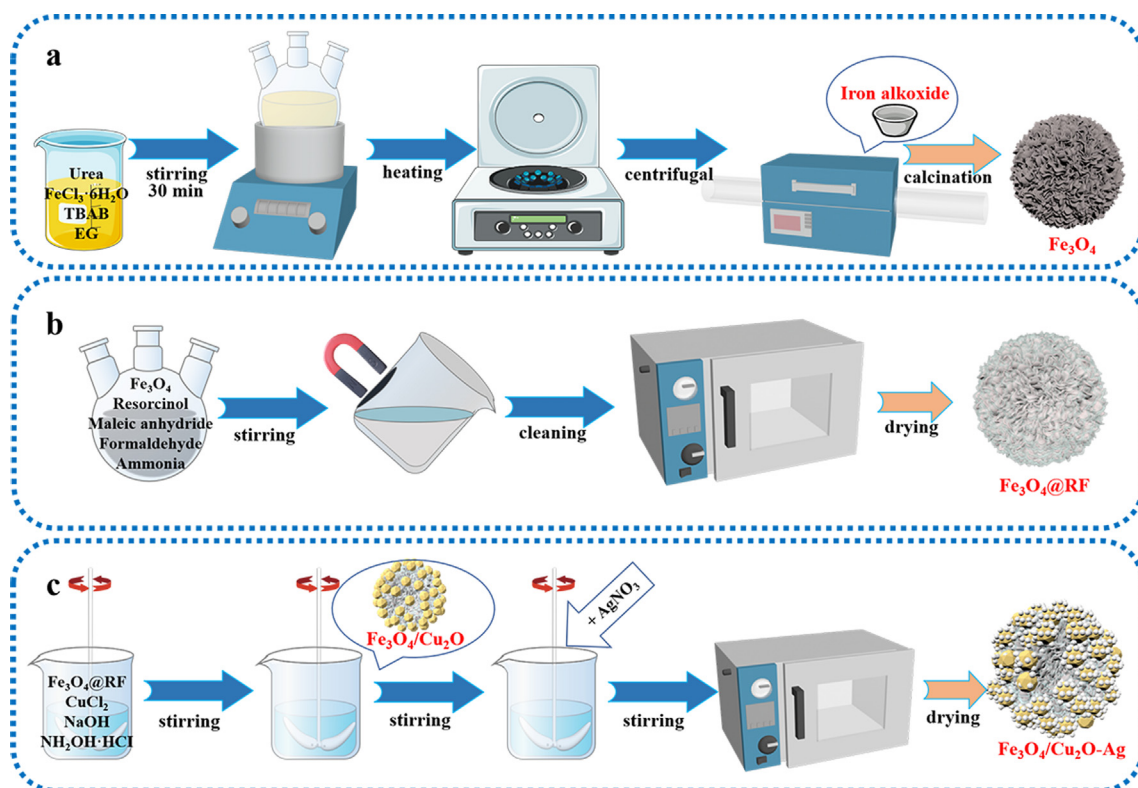
vigorously for 50 min to obtain  $\text{Fe}_3\text{O}_4/\text{Cu}_2\text{O}$  NCs. Here, NaOH and  $\text{NH}_2\text{OH}\cdot\text{HCl}$  were employed as precipitant and reducing agent, respectively. In order to further acquire the  $\text{Fe}_3\text{O}_4/\text{Cu}_2\text{O}$ -Ag NCs, different volumes of  $\text{AgNO}_3$  solution (0.1 M; 1, 2 and 3 mL) were added to the above systems, respectively. After the mixture was stirred for 40 min, the deposit was washed dried. Lastly, the  $\text{Fe}_3\text{O}_4/\text{Cu}_2\text{O}$ -Ag NCs with different Ag loading amounts were prepared and labeled as FCA-1, FCA-2 and FCA-3, respectively.

### 2.3. FDTD algorithm method

The information about FDTD software and parameters are described in [Supplementary Materials](#).

### 2.4. SERS measurements

For investigating the influences of Ag content on SERS signals and thus ascertaining an optimal SERS substrate,  $\text{Fe}_3\text{O}_4/\text{Cu}_2\text{O}$ -Ag NCs with various Ag loading amounts were acted as SERS substrates for detection of reporter molecule (4-MBA). 1 mg of FCA-1, FCA-2 and FCA-3 NCs was added into 3 mL of 4-MBA solution ( $10^{-4}$  M), respectively. Then, the mixture was blended and shaken on an oscillator without light condition for several hours. The 4-MBA-bound samples were centrifuged, washed with ethanol to dislodge the uncombined 4-MBA molecules and then dried for following SERS detection. SERS spectroscopy was performed at 633 nm laser with an energy density of 10 mW. The SERS spectra of the system were scanned between 800 and  $1700\text{ cm}^{-1}$  and acquisition time was about 10 s. According to SERS results, FCA-2 was determined as optimal SERS substrate, which was chosen as SERS substrate to detect SERS spectra of Nap, BaP, Pyr and Ant. SERS detection process of Nap, BaP, Pyr and Ant was the same as the above SERS detection of 4-MBA. Furthermore, SERS spectra of 4-MBA were acquired at 20 random spots on FCA-2 to evaluate



**Scheme 1.** Schematic diagram of synthetic steps for  $\text{Fe}_3\text{O}_4$  (a),  $\text{Fe}_3\text{O}_4@\text{RF}$  nanocrystals (b),  $\text{Fe}_3\text{O}_4/\text{Cu}_2\text{O}$  and  $\text{Fe}_3\text{O}_4/\text{Cu}_2\text{O}$ -Ag NCs (c).



the uniformity of SERS signal. For obtaining the limit of detection (LOD) of Nap, BaP, Pyr and Ant, these four stock solutions were deliquated to different concentrations ( $10^{-4}$  M –  $10^{-11}$  M), respectively. The LOD was measured with the above procedures. To evaluate the practicalities of  $\text{Fe}_3\text{O}_4/\text{Cu}_2\text{O}$ -Ag NCs, SERS spectra of PAHs in soil were achieved, given that soils were typical carriers containing these persistent organic pollutants.

## 2.5. Photocurrent response measurements

Standard three-electrode circuit was employed to analyze photocurrent response in a CHI660D electrochemical workstation. Ag/AgCl, platinum wire and  $\text{Fe}_3\text{O}_4/\text{Cu}_2\text{O}$ -Ag NCs were chosen as reference electrode, counter electrode and working electrode, respectively.  $\text{Na}_2\text{SO}_4$  aqueous solution (0.5 M) was used as electrolyte. 0.003 g of photocatalyst powder and 0.01 g of PVP were blended with 3  $\mu\text{L}$  of absolute ethanol and 3  $\mu\text{L}$  of oleic acid. After continuous ultrasonic blending for 30 min, the slurry was formed and then was evenly coated on the ITO glass. For enhancing the adhesion, the ITO glass was heated to the certain high temperature for several hours.

## 2.6. Photocatalytic experiments

For investigating the influence of Ag loading on photocatalytic activity and thus determining an optimal photocatalyst,  $\text{Fe}_3\text{O}_4/\text{Cu}_2\text{O}$ -Ag NCs with different Ag loading amounts were also acted as photocatalysts for catalytic degradation of PAHs. Firstly, 50 mg of  $\text{Fe}_3\text{O}_4/\text{Cu}_2\text{O}$ , FCA-1, FCA-2 and FCA-3 NCs was put into 100 mL of Nap solution (5 mg/L), respectively. 4 mL of aqueous combination was extracted and leached via a 0.22 mm filter for further analysis in a time interval. In order to prove the fact that Nap was degraded by photocatalysis rather than spontaneous degradation, we monitored degradation process of Nap with or without light. According to photocatalytic results, FCA-2 was identified as an optimal photocatalyst and was used to catalyze the reduction of BaP and Ant. Photocatalytic experiments of BaP and Ant were similar to described photocatalyzed process of Nap.

# 3. Results and discussion

## 3.1. Synthesis and characterization of $\text{Fe}_3\text{O}_4/\text{Cu}_2\text{O}$ -Ag NCs

Morphologies of iron alkoxide precursors,  $\text{Fe}_3\text{O}_4$ ,  $\text{Fe}_3\text{O}_4/\text{RF}$  nanocrystals,  $\text{Fe}_3\text{O}_4/\text{Cu}_2\text{O}$  NCs and  $\text{Fe}_3\text{O}_4/\text{Cu}_2\text{O}$ -Ag NCs were examined by SEM. As shown in **Figure S1a1**, iron alkoxide precursors exhibit flower ball-like shapes. Flower ball-like  $\text{Fe}_3\text{O}_4$  nanocrystals can be obtained by calcining iron alkoxide precursors (**Figure S1a2**).  $\text{Fe}_3\text{O}_4/\text{RF}$  nanocrystals still maintain flower ball-like structures after  $\text{Fe}_3\text{O}_4$  nanocrystals are modified with RF layers, and surfaces of the  $\text{Fe}_3\text{O}_4$  nanocrystals become smoother (**Figure S1a3**). As presented in **Figure S1a4**,  $\text{Cu}_2\text{O}$  (~150 nm) truncated octahedron nanocrystals are successfully decorated on  $\text{Fe}_3\text{O}_4/\text{RF}$  nanocrystals. **Figure S1a5** is SEM image of  $\text{Fe}_3\text{O}_4/\text{Cu}_2\text{O}$ -Ag NCs. Grain size of Ag nanocrystals is too small (~5 nm), and it is difficult to distinguish them from  $\text{Fe}_3\text{O}_4/\text{Cu}_2\text{O}$ -Ag NCs. For verifying the existence of Ag nanocrystals, EDS elemental mapping was carried out. According to the EDS elemental analysis results in **Figure S1c** recorded from the red box in **Figure S1a5**, elements of Fe, Cu, O and Ag are randomly and homogeneously distributed in  $\text{Fe}_3\text{O}_4/\text{Cu}_2\text{O}$ -Ag NCs, which strongly confirms the formation of Ag nanocrystals. Apart from SEM images, XRD technology was used for structural characterization of  $\text{Fe}_3\text{O}_4$  nanocrystals,  $\text{Fe}_3\text{O}_4/\text{Cu}_2\text{O}$  NCs and  $\text{Fe}_3\text{O}_4/\text{Cu}_2\text{O}$ -Ag NCs. As illustrated in **Figure S1b**, typical diffraction peaks of  $\text{Fe}_3\text{O}_4$  nanocrystals located at  $2\theta$  values of  $30.1^\circ$ ,  $35.4^\circ$ ,

$43.0^\circ$ ,  $53.4^\circ$ ,  $56.9^\circ$ , and  $62.5^\circ$  are indexed to (220), (311), (400), (422), (511) and (440) crystalline planes of  $\text{Fe}_3\text{O}_4$  (JCPDS 85-1436), respectively [46]. No other impurities are detected. It is worthwhile to note that it is not sufficient to determine formation of  $\text{Fe}_3\text{O}_4$  only by XRD, for the reason that  $\text{Fe}_3\text{O}_4$  and  $\gamma\text{-Fe}_2\text{O}_3$  have almost the identical crystal structure [47]. Therefore, Mössbauer spectroscopy measurements were carried out to further confirm existence of  $\text{Fe}_3\text{O}_4$ . Mössbauer spectrum and corresponding Mössbauer spectrum parameters of flower ball-like  $\text{Fe}_3\text{O}_4$  nanocrystals are presented in **Figure S2** and **Table S1**. Mössbauer spectrum can be fitted into two Zeeman sextets. Sharp and significant lines of magnetic sextets exhibit a double six peak structure, which is the typical characteristic of  $\text{Fe}_3\text{O}_4$  [48,49]. Hyperfine field is 48.9 and 45.8 Tesla, and the isomer displacement is 0.311 and 0.570 mm/s, corresponding to  $\text{Fe}^{2+}$  and  $\text{Fe}^{3+}$  in octahedral interstitial sites and  $\text{Fe}^{3+}$  in tetrahedral interstitial sites. After  $\text{Cu}_2\text{O}$  nanocrystals are successfully modified on surfaces of  $\text{Fe}_3\text{O}_4$ , four new XRD peaks are founded at  $2\theta$  values of  $36.4^\circ$ ,  $42.2^\circ$  and  $61.2^\circ$ , which are assigned to (111), (200), and (220) planes of  $\text{Cu}_2\text{O}$  (JCPDS 05-0667) [50]. As for  $\text{Fe}_3\text{O}_4/\text{Cu}_2\text{O}$ -Ag NCs, additional three XRD peaks are observed at  $2\theta$  values of  $38.0^\circ$ ,  $44.2^\circ$  and  $66.5^\circ$ , which correspond to (111), (200), and (220) planes of Ag (JCPDS 04-0783) [51]. XPS technology was applied to ascertain the valence of elements in  $\text{Fe}_3\text{O}_4/\text{Cu}_2\text{O}$ -Ag NCs. Full XPS spectra of  $\text{Fe}_3\text{O}_4$  nanocrystals,  $\text{Fe}_3\text{O}_4/\text{Cu}_2\text{O}$  and  $\text{Fe}_3\text{O}_4/\text{Cu}_2\text{O}$ -Ag NCs are exhibited in **Figure S3**. Fe 2p, Cu 2p, Ag 3d, C 1s and O 1s are observed and no impurity is found within detection limit of XPS. High-resolution XPS spectra of Fe 2p, Cu 2p and Ag 3d are shown in **Figure S4**. Fe 2p spectra in **Figure S4a** display a prominent peak at 710.2 eV and a comparatively weak peak at 723.4 eV for three samples, which are attributed to characteristics of Fe  $2p_{3/2}$  and Fe  $2p_{1/2}$  in  $\text{Fe}_3\text{O}_4$  [52,53]. Cu 2p XPS spectra for  $\text{Fe}_3\text{O}_4/\text{Cu}_2\text{O}$  and  $\text{Fe}_3\text{O}_4/\text{Cu}_2\text{O}$ -Ag NCs in **Figure S4b** show two main peaks at 952.6 and 932.6 eV, which are ascribed to Cu  $2p_{1/2}$  and Cu  $2p_{3/2}$  of  $\text{Cu}^+$  in  $\text{Cu}_2\text{O}$  [54,55]. As depicted in **Figure S4c**, peaks of  $\text{Fe}_3\text{O}_4/\text{Cu}_2\text{O}$ -Ag NCs at 374.2 and 368.2 eV with a spin-orbit splitting of 6 eV are assigned to Ag  $3d_{3/2}$  and Ag  $3d_{5/2}$  of metallic silver [56]. Notably, binding energies of Cu 2p in  $\text{Fe}_3\text{O}_4/\text{Cu}_2\text{O}$ -Ag NCs are slightly higher than those in the  $\text{Fe}_3\text{O}_4/\text{Cu}_2\text{O}$  NCs, which can be attributed to the charge transfer between  $\text{Cu}_2\text{O}$  and Ag [57]. In addition, the modification of Ag on the surfaces of the  $\text{Fe}_3\text{O}_4/\text{Cu}_2\text{O}$  NCs results in the peak intensity of Cu 2p. Therefore, the results obtained from SEM, XRD, Mössbauer and XPS confirm successful preparation of  $\text{Fe}_3\text{O}_4$  nanocrystals,  $\text{Fe}_3\text{O}_4/\text{Cu}_2\text{O}$  NCs and  $\text{Fe}_3\text{O}_4/\text{Cu}_2\text{O}$ -Ag NCs.

## 3.2. Optimization of $\text{Fe}_3\text{O}_4/\text{Cu}_2\text{O}$ -Ag NCs substrates

For determining the optimal SERS substrate, the number of Ag on  $\text{Fe}_3\text{O}_4/\text{Cu}_2\text{O}$  NCs was adjusted by adding various amounts of  $\text{AgNO}_3$ . As exhibited in **Fig. 1a1** and **a2**, when the addition amount of  $\text{AgNO}_3$  changes from 1 to 2 mL, the surfaces of  $\text{Cu}_2\text{O}$  become rougher owing to the increase of Ag absorbed on the surfaces. Self-aggregation of Ag can be observed obviously when the amount of  $\text{AgNO}_3$  further increases to 3 mL (**Fig. 1a3**) [58]. To reveal changes of microstructure and elemental distributions when increasing Ag contents,  $\text{Fe}_3\text{O}_4/\text{Cu}_2\text{O}$ -Ag NCs were measured by TEM, high angle annular dark-field (HAADF) STEM and EDS elemental mapping. It can be seen from **Fig. 1b** and **1c** that  $\text{Fe}_3\text{O}_4$  nanocrystals with a diameter of about 1.5  $\mu\text{m}$  are located at the center of  $\text{Fe}_3\text{O}_4/\text{Cu}_2\text{O}$  NCs and are surrounded with  $\text{Cu}_2\text{O}$  and Ag nanocrystals. Ag nanocrystals on surfaces of  $\text{Fe}_3\text{O}_4/\text{Cu}_2\text{O}$  NCs increase significantly with increase of Ag addition. However, excessive Ag loading results in aggregation and coalescence of Ag nanocrystals. Given that SERS enhancement ability is dependent upon the number of noble metal nanocrystals and the spacing between noble metal nanocrystals [59], SERS performance of

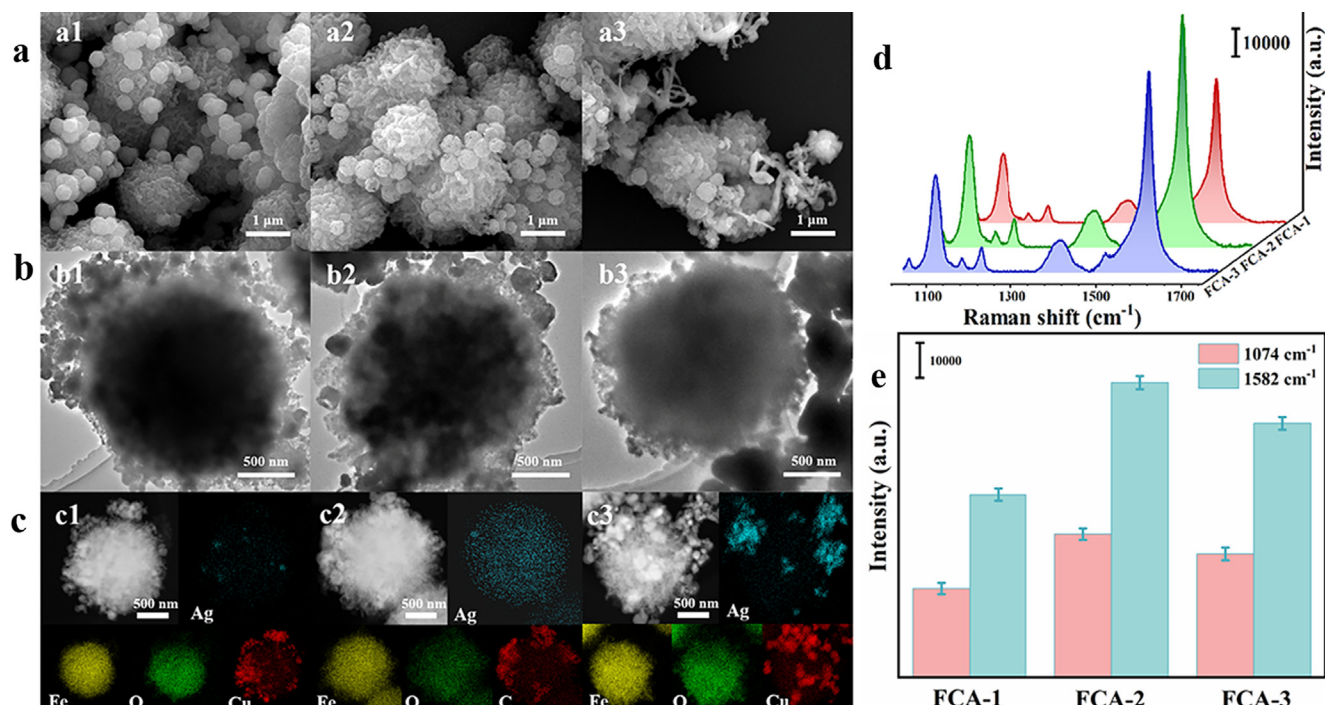


**Fig. 1.** SEM, TEM, HAADF-STEM images and corresponding EDS elemental mapping results (Ag, Fe, O and Cu) of  $\text{Fe}_3\text{O}_4/\text{Cu}_2\text{O}$ -Ag NCs (FCA-1) (a1, b1, c1), (FCA-2) (a2, b2, c2) and (FCA-3) (a3, b3, c3); SERS spectra of 4-MBA ( $10^{-4}$  M) on FCA-1, FCA-2 and FCA-3 NCs (d) and the histograms of SERS signals of 4-MBA at  $1074\text{ cm}^{-1}$  and  $1582\text{ cm}^{-1}$  (e).

$\text{Fe}_3\text{O}_4/\text{Cu}_2\text{O}$ -Ag NCs with different Ag contents was evaluated. 4-MBA ( $10^{-4}$  M) was acted as a reporter molecule to explore relationship between Ag content and SERS signal intensity, as presented in Fig. 1d. Detailed band assignments of 4-MBA SERS spectra are presented in Table S2 [60]. Fig. 1e illustrates SERS intensity of 4-MBA adsorbed on the  $\text{Fe}_3\text{O}_4/\text{Cu}_2\text{O}$ -Ag NCs at  $1074\text{ cm}^{-1}$  and  $1582\text{ cm}^{-1}$ . And error bar represents standard deviation obtained from five independent tests. The SERS intensity of 4-MBA rises up and then declines with increasing content of Ag nanocrystals (Fig. 1e), and 4-MBA adsorbed on FCA-2 NCs has a higher SERS intensity compared with FCA-1 and FCA-3 NCs. This phenomenon is to be expected and will be discussed below.

### 3.3. Mechanism of SERS enhancement by $\text{Fe}_3\text{O}_4/\text{Cu}_2\text{O}$ -Ag NCs

EM mechanism is generally considered to play a major part in SERS enhancement, which mainly derives from excitation of LSPR on noble metal nanostructures [61–63]. Especially, owing to the coupling effect between noble metal nanocrystals, stronger electromagnetic fields will be generated in/between adjacent noble

metal nanocrystals, called “hot spots”, so as to considerably enhance SERS signals of target molecules [64]. One clear reason is that multiple collisions between the photons excited by incident light and noble metals nanocrystals can improve SERS signal intensity [65]. As displayed in Fig. 2a, the electromagnetic field intensity dispersion of FCA-2 NCs under periodic boundary conditions was simulated and analyzed by FDTD method, where a large number of hot spots are located in the gap between Ag nanocrystals. Because number of Ag nanocrystals on surface of FCA-2 NCs is more than that of FCA-1 NCs, FCA-2 NCs have more “hot spots”. Given that SERS signal intensity relies on amount of “hot spots” in SERS substrates, it is reasonable that FCA-2 NCs have better SERS performance than FCA-1 NCs [66,67]. Furthermore, unexpected decrease of SERS signal on FCA-3 NCs can be attributed to the excessive addition of Ag nanocrystals, which results in agglomeration of Ag nanocrystals and thus decreases the number of “hot spots” [59]. CE also makes contribution to SERS enhancement through CT between adsorbed molecules and SERS substrates [68]. It is well known that SERS peaks of 4-MBA mainly include  $a_1$  symmetric vibration modes and  $b_2$  asymmetric vibration modes,

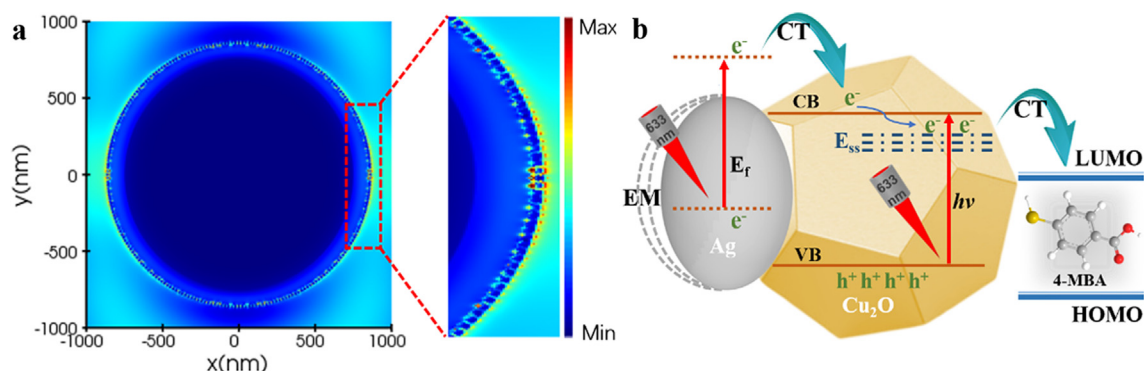


**Fig. 2.** Electric field distribution of FCA-2 NCs simulated by FDTD method (a) and schematic diagram of CT between 4-MBA and  $\text{Fe}_3\text{O}_4/\text{Cu}_2\text{O}$ -Ag NCs (b).

in which enhancement of  $b_2$  vibration modes originates from CT between substrates and 4-MBA [69,70]. The  $b_2$  vibration bands of 4-MBA absorbed on  $\text{Fe}_3\text{O}_4/\text{Cu}_2\text{O}$ -Ag NCs at  $1144\text{ cm}^{-1}$  are clearly observed in Fig. 1d. In order to account for CT process between  $\text{Fe}_3\text{O}_4/\text{Cu}_2\text{O}$ -Ag NCs and 4-MBA, the CT mechanism was proposed, as shown in Fig. 2b. The deposited Ag nanocrystals on  $\text{Cu}_2\text{O}$  surface can be excited by LSPR adsorption. Photoexcited electrons can be injected into the conduction band (CB) of  $\text{Cu}_2\text{O}$  and/or then be vibrantly relaxed to the surface energy levels ( $E_{\text{SS}}$ ) of  $\text{Cu}_2\text{O}$ , and eventually be diverted to the LUMO of 4-MBA. For the present Ag- $\text{Cu}_2\text{O}$ -molecular system, the CB of  $\text{Cu}_2\text{O}$  acts as a “bridge” between Ag (donor) and 4-MBA (receptor), achieving a “donor bridge receptor” CT mode [71,72]. A small quantity of Ag nanocrystals cannot provide enough photoexcited electrons. On the contrary, excess Ag nanocrystals will cover the surfaces of  $\text{Cu}_2\text{O}$  and lead to insufficient light absorption. Therefore, we conclude that the appropriate amount of Ag nanocrystals is crucial to achieve better SERS performance based on both EM and CE mechanism. Herein, an extremely high enhancement factor (EF) of  $3.08 \times 10^6$  was achieved according to the following equation [73,74]:

$$EF = \frac{I_{\text{SERS}} N_{\text{Solid}}}{I_{\text{Solid}} N_{\text{SERS}}} = \frac{I_{\text{SERS}}}{I_{\text{Solid}}} \times \frac{\rho \times h \times S_{\text{laser}} \times N_A / M}{S_{\text{laser}} / S_{4\text{-MBA}}}$$

Specific EF calculation process and Raman intensity (Figure S5) of solid 4-MBA powders are recorded in Supplementary Materials.

### 3.4. Stability and reproducibility of $\text{Fe}_3\text{O}_4/\text{Cu}_2\text{O}$ -Ag NCs

Stability of substrates and reproducibility of SERS signals of target analytes are vitally important in actual application. So as to assess stability of SERS substrates, FCA-2 NCs were stored in a centrifuge tube for 0, 10, 20 and 30 days. Histogram of average SERS intensity of the 4-MBA at  $1074$  and  $1582\text{ cm}^{-1}$  on FCA-2 NCs stored for different times is shown in Figure S6a. There is no significant reduction in SERS intensity of 4-MBA at  $1074$  and  $1582\text{ cm}^{-1}$  even after a month, indicating  $\text{Fe}_3\text{O}_4/\text{Cu}_2\text{O}$ -Ag SERS substrates have good storage stability. For assessing reproducibility of SERS signals, SERS spectra of 20 random points on FCA-2 NCs functionalized with  $10^{-4}\text{ M}$  4-MBA were obtained (Figure S6b). Corresponding relative standard deviation (RSD) of 4-MBA at  $1074$  as well as  $1582\text{ cm}^{-1}$  was calculated by the linear regression method (Figure S6c). Results suggest that all the SERS signals of 4-MBA are highly consistent, and RSD values of 4-MBA at  $1074$  and  $1582\text{ cm}^{-1}$  are 9.73 and 10.82 %, which implies that  $\text{Fe}_3\text{O}_4/\text{Cu}_2\text{O}$ -Ag SERS substrates have high uniformity and excellent spectral reproducibility in a large-scale area.

### 3.5. SERS applications of $\text{Fe}_3\text{O}_4/\text{Cu}_2\text{O}$ -Ag NCs

Four kinds of PAHs (Nap, BaP, Pyr and Ant;  $10^{-11} \sim 10^{-4}\text{ M}$ ) were selected as probe molecules to assess applicability of FCA-2 NCs as SERS substrates for quantitative detection of PAHs. Fig. 3 shows that the characteristic peaks of Nap, BaP, Pyr and Ant can be observed clearly, and LOD of Nap, BaP, Pyr and Ant is as low as  $10^{-9}$ ,  $10^{-9}$ ,  $10^{-9}$  and  $10^{-10}\text{ M}$ , respectively. In addition, relationship between the concentrations of Nap, BaP, Pyr and Ant adsorbed on FCA-2 NCs and the corresponding SERS intensity at  $1379$ ,  $1555$ ,  $1599$  and  $1380\text{ cm}^{-1}$  are illustrated in Figure S7. SERS intensity for four kinds of PAHs follows linear relationship versus the logarithm of the concentrations of PAHs and correlation coefficients ( $R^2$ ) are more than 0.97, which indicates that  $\text{Fe}_3\text{O}_4/\text{Cu}_2\text{O}$ -Ag NCs are ultra-sensitive SERS substrates and can realize quantification of different kinds of PAHs down to  $10^{-9}\text{ M}$ .

In order to verify application effect of  $\text{Fe}_3\text{O}_4/\text{Cu}_2\text{O}$ -Ag NCs for PAHs detection in actual environment, soil samples taken from Jilin

Normal University (Changchun China) were detected. The soil samples were heated at  $500\text{ }^\circ\text{C}$  for 3 h to avoid interferences of other soil components on SERS spectra. As exhibited in Fig. 4a, heat-treated soil (20 mg) was added to a centrifuge tube and mixed with four kinds of PAHs (Nap, BaP, Pyr and Ant  $10^{-4}\text{ M}$ , 3 mL) for 2 h, respectively. Subsequently, 1 mg of FCA-2 NCs was added to the above mixtures, respectively. After shaking with an oscillator in dark overnight, PAHs labeled FCA-2 NCs were separated and collected from the mixed solution by a magnet. Finally, PAHs labeled FCA-2 NCs were transferred to clean slides, and SERS signals of the four samples were recorded excited with  $632.8\text{ nm}$  laser. As shown in Fig. 4b, no obvious SERS signals are obtained for the heat-treated soil samples. In contrast, the SERS signals of four kinds of PAHs can be clearly detected, demonstrating that  $\text{Fe}_3\text{O}_4/\text{Cu}_2\text{O}$ -Ag NCs are suitable for the SERS detection of PAHs in the actual environment.

### 3.6. Photocatalytic performance of $\text{Fe}_3\text{O}_4/\text{Cu}_2\text{O}$ -Ag NCs

Efficient photocatalytic degradation of PAHs is another key development goal while achieving ultra-sensitive SERS detection. Given that the separation and transfer ability of photogenerated carriers largely determine photocatalytic performance of photocatalysts, transient photocurrent measurements were implemented to estimate excitation and transfer of photoexcited electron-hole pairs in  $\text{Fe}_3\text{O}_4/\text{Cu}_2\text{O}$ -Ag NCs [75]. Transient photocurrent responses of  $\text{Fe}_3\text{O}_4$  nanocrystals,  $\text{Fe}_3\text{O}_4/\text{Cu}_2\text{O}$  and  $\text{Fe}_3\text{O}_4/\text{Cu}_2\text{O}$ -Ag NCs with different Ag contents (FCA-1, FCA-2 and FCA-3) are presented in Fig. 5a. Under visible light illumination, all samples have quick and reproducible photocurrent response, and photocurrent density decreases rapidly to zero after cessation of light excitation. In addition,  $\text{Fe}_3\text{O}_4/\text{Cu}_2\text{O}$ -Ag NCs have higher photocurrent response than  $\text{Fe}_3\text{O}_4$  nanocrystals and  $\text{Fe}_3\text{O}_4/\text{Cu}_2\text{O}$  NCs, which indicates that introduction of Ag can enhance the separation and transfer ability of electron-hole pairs [57]. It is a remarkable fact that the photocurrent density of  $\text{Fe}_3\text{O}_4/\text{Cu}_2\text{O}$ -Ag NCs increases firstly and then decreases with increase of Ag contents, and reaches a maximum for FCA-2 NCs. A reasonable explanation is that Ag nanocrystals can enhance light absorption owing to LSPR effect of Ag nanocrystals [76,77], but excess Ag nanocrystals are likely to cover surfaces of  $\text{Cu}_2\text{O}$  entirely, which will inhibit generation of photoexcited carriers and thus lead to poor photocatalytic activity [78]. Photoluminescence (PL) spectroscopy was used to further assess recombination of photoexcited carriers for  $\text{Fe}_3\text{O}_4/\text{Cu}_2\text{O}$ -Ag NCs. As depicted in Fig. 5b, FCA-2 NCs exhibit the lowest PL intensity owing to slowest recombination of charge carries, and this trend is in accordance with above transient photocurrent response result, which provides further evidence that FCA-2 NCs have the highest carrier separation and transfer efficiency [79].

UV-vis DRS was used to explore the effect of Ag nanocrystals on photocatalytic performance of  $\text{Fe}_3\text{O}_4/\text{Cu}_2\text{O}$  NCs. As illustrated in Fig. 5c, absorption peaks ( $450\text{--}500\text{ nm}$ ) of both  $\text{Fe}_3\text{O}_4/\text{Cu}_2\text{O}$  and FCA-2 NCs appear in visible light region. With the addition of Ag nanocrystals, FCA-2 NCs show stronger visible light absorption compared with  $\text{Fe}_3\text{O}_4/\text{Cu}_2\text{O}$  NCs, which is ascribed to SPR effect of Ag nanocrystals [80]. Values of band gap energy ( $E_g$ ) of  $\text{Fe}_3\text{O}_4/\text{Cu}_2\text{O}$  and FCA-2 NCs were calculated according to experiential Tauc's formula[81]:

$$(\alpha h\nu)^2 = A(h\nu - E_g)$$

Where  $E_g$ ,  $\alpha$ ,  $h\nu$  and  $A$  stand for band gap energy, absorbance, photon energy and constant, respectively. As exhibited in Fig. 5d, the  $E_g$  is determined from intercept of tangent of  $(\alpha h\nu)^2$  versus  $h\nu$  curves. Accordingly,  $E_g$  of  $\text{Fe}_3\text{O}_4/\text{Cu}_2\text{O}$  and FCA-2 NCs is computed to be around 2.32 and 2.23 eV, respectively. Above results



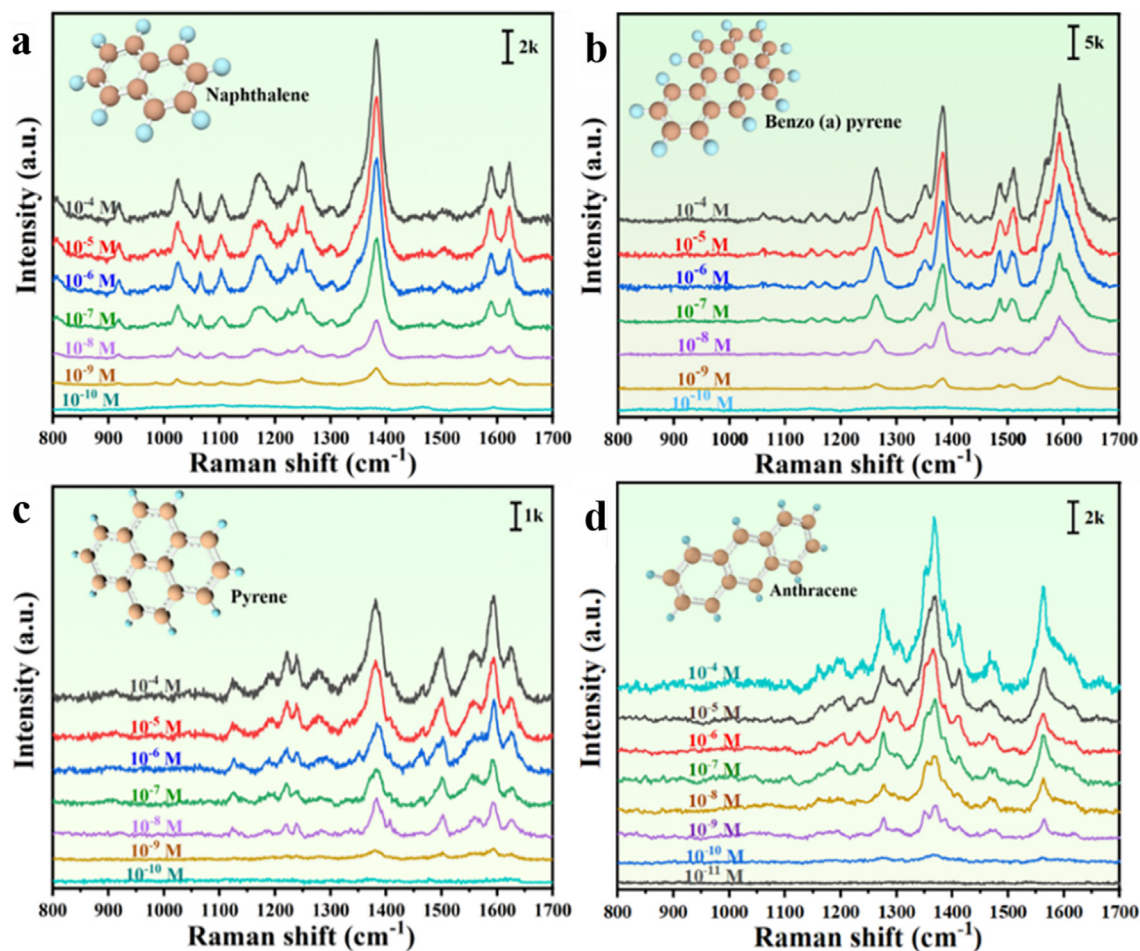


Fig. 3. SERS spectra of Nap (a), BaP (b), Pyr (c) and Ant (d) with different concentrations ( $10^{-11} \sim 10^{-4}$  M) adsorbed on FCA-2 NCs.

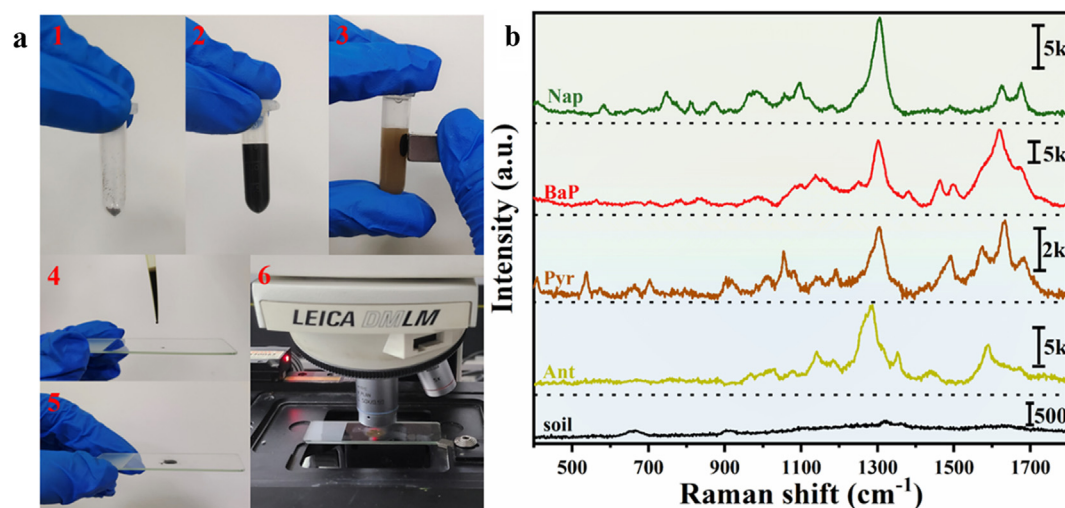
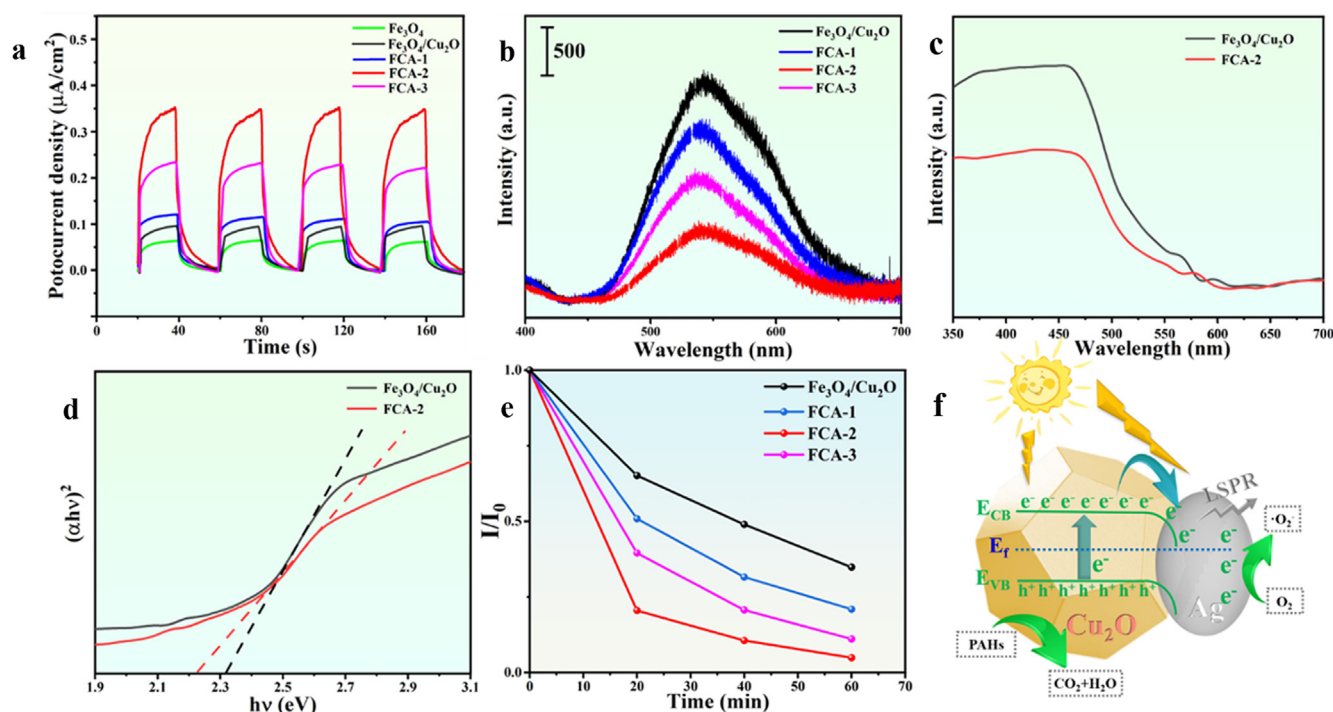


Fig. 4. Operation procedure of SERS detection of PAHs in soil using FCA-2 NCs as SERS substrates (a) and SERS spectra of Nap, BaP, Pyr, Ant and heat-treated soil (b).

indicate that the  $\text{Fe}_3\text{O}_4/\text{Cu}_2\text{O}$ -Ag NCs (FCA-2 NCs) with a reduced bandgap of 0.09 eV result in an increased visible light response [82].

For intuitively reflecting the catalytic performance of  $\text{Fe}_3\text{O}_4/\text{Cu}_2\text{O}$  with various loading amounts of Ag nanocrystals, photocatalytic degradation of Nap solution (5 mg/L) catalyzed by  $\text{Fe}_3\text{O}_4/\text{Cu}_2\text{O}$ , FCA-1, FCA-2 and FCA-3 NCs was monitored by SERS spectra

(Fig. 5e).  $I_0$  is regarded as initial SERS intensity of Nap solution at 1379  $\text{cm}^{-1}$  and  $I$  is SERS intensity after irradiation under visible light, respectively. It can be observed that all  $I/I_0$  values decrease with the rise of illumination time and the  $I/I_0$  value of  $\text{Fe}_3\text{O}_4/\text{Cu}_2\text{O}$ -Ag NCs decline faster than that of  $\text{Fe}_3\text{O}_4/\text{Cu}_2\text{O}$  NCs, suggesting addition of Ag nanocrystals promotes degradation of Nap. Moreover, FCA-2 NCs exhibit the highest photocatalytic activity



**Fig. 5.** Photocurrent response of Fe<sub>3</sub>O<sub>4</sub> nanocrystals, Fe<sub>3</sub>O<sub>4</sub>/Cu<sub>2</sub>O, FCA-1, FCA-2 and FCA-3 NCs (a); PL spectra of Fe<sub>3</sub>O<sub>4</sub>/Cu<sub>2</sub>O, FCA-1, FCA-2 and FCA-3 NCs (b); UV-vis DRS (c) and relative band gap energy (d) of Fe<sub>3</sub>O<sub>4</sub>/Cu<sub>2</sub>O and FCA-2 NCs;  $I/I_0$  of SERS signals at 1379  $\text{cm}^{-1}$  of Nap (5 mg/L) versus reaction time in the presence of Fe<sub>3</sub>O<sub>4</sub>/Cu<sub>2</sub>O, FCA-1, FCA-2 and FCA-3 NCs (e) and schematic of photocatalytic degradation mechanism of Fe<sub>3</sub>O<sub>4</sub>/Cu<sub>2</sub>O-Ag NCs for PAHs under visible light illumination (f).

as expected, and degradation rate of Nap by FCA-2 NCs exceeds 95 % after 60 min of illumination. In order to rule out the possibility of spontaneous degradation of Nap, we monitored the degradation process of Nap with or without light, and the histogram of SERS intensity of Nap at 1379  $\text{cm}^{-1}$  is shown in Figure S8. Catalytic degradation of Nap is achieved only with light irradiation, and slight decrease of SERS intensity with no-light condition is attributed to trace adsorption of nanocatalysts.

### 3.7. Mechanism of photocatalytic degradation by Fe<sub>3</sub>O<sub>4</sub>/Cu<sub>2</sub>O-Ag NCs

On the basis of points discussed above, a possible photocatalytic degradation mechanism of Fe<sub>3</sub>O<sub>4</sub>/Cu<sub>2</sub>O-Ag NCs for PAHs was proposed in Fig. 5f. Once two kinds of nanomaterials (Cu<sub>2</sub>O and Ag) with different work functions come into contact with each other, a Schottky barrier forms at Cu<sub>2</sub>O-Ag interface [83,84]. Electrons will migrate from Ag with lower work function to Cu<sub>2</sub>O with higher work function until Fermi level equilibration takes place. Meanwhile, shift-down of Fermi level of Ag and the shift-up of Fermi level of Cu<sub>2</sub>O will result in energy band bending downward. When Fe<sub>3</sub>O<sub>4</sub>/Cu<sub>2</sub>O-Ag NCs are excited by visible light, the photoexcited electrons will transfer from VB of Cu<sub>2</sub>O to CB, while leaving an equal number of holes in VB to form the photoexcited electron-hole pairs. Considering the CB of Cu<sub>2</sub>O is higher than that of new equilibrium Fermi level, photoexcited electrons will continue to transfer from CB of Cu<sub>2</sub>O to Ag. However, photoexcited electrons in Ag nanocrystals cannot be migrated to Cu<sub>2</sub>O because of the blocking effect of Schottky barrier [85]. Therefore, Ag nanocrystals serve as electron traps to efficiently inhibit the recombination of electron-hole pairs. Photoexcited electrons of Ag surfaces can be captured by the adsorbed O<sub>2</sub> to generate superoxide anion radicals ( $\cdot\text{O}_2^-$ ) with strong oxidative capacity for degradation of PAHs [78]. In addition, the holes left in VB of Cu<sub>2</sub>O lead to direct degradation of PAHs molecules. It is worth noting that Ag nanocrystals with LSPR properties can enhance carrier concentration by facilitating

generation of photoexcited electrons and holes, which is also beneficial for degrading the PAHs [86]. In summary, Ag nanocrystals not only promote the formation of active radicals, but also improve light utilization in Fe<sub>3</sub>O<sub>4</sub>/Cu<sub>2</sub>O-Ag NCs. Therefore, it is reasonable that Fe<sub>3</sub>O<sub>4</sub>/Cu<sub>2</sub>O-Ag NCs present better photocatalytic performance than Fe<sub>3</sub>O<sub>4</sub>/Cu<sub>2</sub>O NCs.

### 3.8. Photocatalytic applications of Fe<sub>3</sub>O<sub>4</sub>/Cu<sub>2</sub>O-Ag NCs

So as to evaluate applicability of Fe<sub>3</sub>O<sub>4</sub>/Cu<sub>2</sub>O-Ag NCs for visible light-driven degradation of different PAHs, in addition to Nap, BaP and Ant were also selected as degradation targets to perform same photocatalytic experiments under visible light irradiation. SERS spectral changes at various times during photocatalytic process were monitored by Raman spectrometer. As presented in Figure S9, it is detected that intensity of SERS peaks of Nap, BaP and Ant decreases in different degrees with increasing irradiation time. Especially, it can also be seen that the position and shape of SERS peaks of PAHs change slightly in the photocatalytic process, which may be due to formation of complex intermediates in the photocatalytic process [87,88]. In order to intuitively reflect changes in SERS signal intensity, the temporal variations of  $I/I_0$  for SERS peaks of Nap (1379  $\text{cm}^{-1}$ ), BaP (1555  $\text{cm}^{-1}$ ) and Ant (1380  $\text{cm}^{-1}$ ) catalyzed by FCA-2 NCs are plotted in Fig. 6a. Characteristic SERS signals of Nap, BaP and Ant almost completely disappear within 60, 140 and 180 min, respectively. Furthermore, the degradation efficiency of Nap, BaP and Ant was calculated by plotting natural logarithm of  $I/I_0$  versus irradiation time, as shown in Fig. 6b. About 80 % of Nap can be degraded on FCA-2 NCs within 20 min, while degradation of same amount of BaP and Nap is achieved within 100 and 120 min, respectively. Although FCA-2 NCs exhibit different catalytic activities towards three PAHs, real-time monitoring of degradation of PAHs catalyzed by FCA-2 NCs clearly indicates that Fe<sub>3</sub>O<sub>4</sub>/Cu<sub>2</sub>O-Ag NCs can achieve catalytic degradation of multiple PAHs.



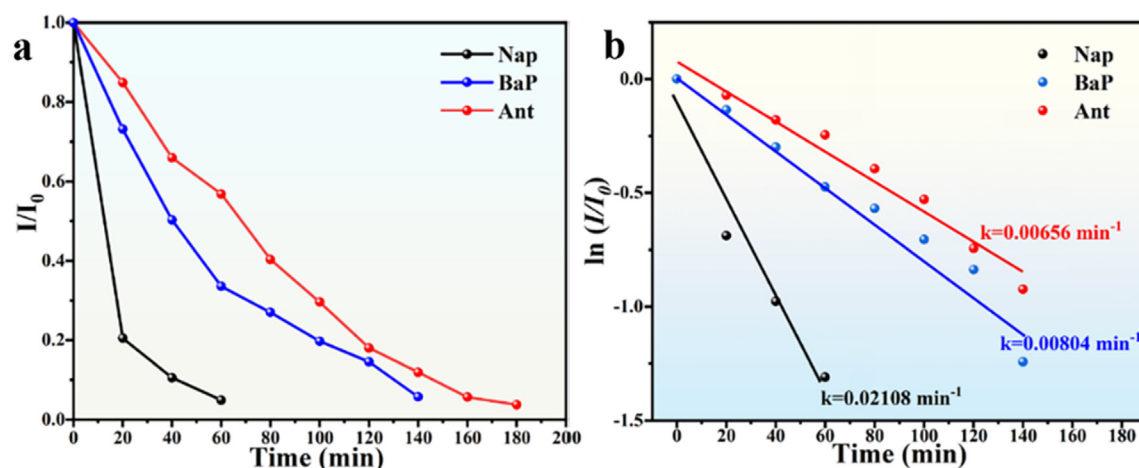


**Fig. 6.** The plots of  $I/I_0$  for the SERS peaks of Nap ( $1379 \text{ cm}^{-1}$ ), BaP ( $1555 \text{ cm}^{-1}$ ) and Ant ( $1380 \text{ cm}^{-1}$ ) catalyzed by FCA-2 NCs versus illumination time (a) and the corresponding plots of  $\ln(I/I_0)$  versus reaction time (b).

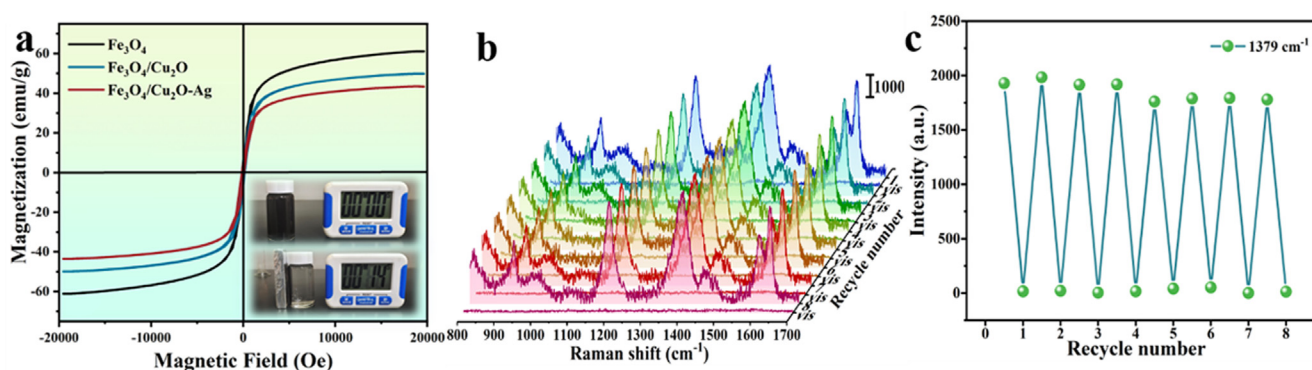


**Fig. 7.** Magnetic hysteresis ( $M-H$ ) loops of  $\text{Fe}_3\text{O}_4$  nanocrystals,  $\text{Fe}_3\text{O}_4/\text{Cu}_2\text{O}$  and  $\text{Fe}_3\text{O}_4/\text{Cu}_2\text{O-Ag}$  NCs (The inset is photograph of  $\text{Fe}_3\text{O}_4/\text{Cu}_2\text{O-Ag}$  NCs scattered in water before and after magnetic separation) (a); SERS spectra of Nap (5 mg/L) (b) and their SERS intensities at  $1379 \text{ cm}^{-1}$  (c) during eight cycles of visible light-driven photocatalysis.

### 3.9. Magnetic applications of $\text{Fe}_3\text{O}_4/\text{Cu}_2\text{O-Ag}$ NCs

Magnetic properties of  $\text{Fe}_3\text{O}_4$  nanocrystals,  $\text{Fe}_3\text{O}_4/\text{Cu}_2\text{O}$  and  $\text{Fe}_3\text{O}_4/\text{Cu}_2\text{O-Ag}$  NCs (FCA-2 NCs) were tested at room temperature, and their magnetic hysteresis ( $M-H$ ) loops are verified in Fig. 7a. It is found that  $\text{Fe}_3\text{O}_4$  nanocrystals,  $\text{Fe}_3\text{O}_4/\text{Cu}_2\text{O}$  and  $\text{Fe}_3\text{O}_4/\text{Cu}_2\text{O-Ag}$  NCs possess superparamagnetic, and their saturation magnetization ( $M_s$ ) values are  $61.0$ ,  $50.8$  and  $41.2 \text{ emu}\cdot\text{g}^{-1}$ , respectively. Compared with  $\text{Fe}_3\text{O}_4$  nanocrystals, decreased  $M_s$  value of  $\text{Fe}_3\text{O}_4/\text{Cu}_2\text{O}$  and  $\text{Fe}_3\text{O}_4/\text{Cu}_2\text{O-Ag}$  NCs is attributed to increased mass of  $\text{Cu}_2\text{O}$  nanocrystals and  $\text{Cu}_2\text{O-Ag}$  NCs [89]. However, even though  $\text{Fe}_3\text{O}_4/\text{Cu}_2\text{O-Ag}$  NCs have lowest  $M_s$  value, they are collected by the magnet within 14 s, as shown in the inset of Fig. 7a. Excellent magnetic response property endows  $\text{Fe}_3\text{O}_4/\text{Cu}_2\text{O-Ag}$  NCs with capability of recovery and reuse. So as to further assess the stability and reusability of  $\text{Fe}_3\text{O}_4/\text{Cu}_2\text{O-Ag}$  NCs, sequential SERS detection and photodegradation experiments of Nap (5 mg/L) adsorbed on  $\text{Fe}_3\text{O}_4/\text{Cu}_2\text{O-Ag}$  NCs were carried out. As reflected in Fig. 7b, the SERS peaks of Nap disappear after visible light irradiation, and  $\text{Fe}_3\text{O}_4/\text{Cu}_2\text{O-Ag}$  NCs still maintain an excellent SERS activity even after 8 cycles. To intuitively show change of SERS intensity, the SERS intensities of Nap at  $1379 \text{ cm}^{-1}$  after eight cycles for detection/photodegradation of Nap are exhibited in Fig. 7c. The  $\text{Fe}_3\text{O}_4/\text{Cu}_2\text{O-Ag}$  NCs almost maintain their initial SERS activity in the first 4 cycles. Slight decrease of the SERS signals after 4 cycles may be responsible for the loss of  $\text{Fe}_3\text{O}_4/\text{Cu}_2\text{O-Ag}$  NCs or reduction of their adsorption capacity during cycling process. However, they still

maintain nearly 90 % of the initial SERS activity even after 8 cycles. To sum up, it can draw a conclusion that our proposed  $\text{Fe}_3\text{O}_4/\text{Cu}_2\text{O-Ag}$  NCs are fully recycled and thus have great potential for applications in efficient detection and catalytic degradation of PAHs.

## 4. Conclusions

In conclusion, magnetic multifunctional  $\text{Fe}_3\text{O}_4/\text{Cu}_2\text{O-Ag}$  NCs for ultra-sensitive SERS detection and efficient photocatalytic degradation of PAHs have been successfully developed. Ag amounts on surfaces of  $\text{Fe}_3\text{O}_4/\text{Cu}_2\text{O-Ag}$  NCs were adjusted and 4-MBA was chosen as reporter molecule to investigate the effect of Ag contents on SERS signal intensity. It was observed that SERS intensity of 4-MBA first increased and then decreased when increasing content of Ag nanocrystals, which depended on the numbers of “hot spots” as well as photoexcited electrons in SERS substrates. In addition, little changes in SERS intensity of 4-MBA were found even after a month, suggesting that the  $\text{Fe}_3\text{O}_4/\text{Cu}_2\text{O-Ag}$  substrates had good stability. Four kinds of PAHs (Nap, BaP, Pyr and Ant) were used to evaluate applicability of  $\text{Fe}_3\text{O}_4/\text{Cu}_2\text{O-Ag}$  as SERS substrates. When the concentrations of PAHs ranged from  $10^{-11}$  to  $10^{-4} \text{ M}$ , SERS intensity of Nap, BaP, Pyr and Ant followed linear relationship versus the logarithm of the concentrations of PAHs, and LOD of Nap, BaP, Pyr and Ant was as low as  $10^{-9}$ ,  $10^{-9}$ ,  $10^{-9}$  and  $10^{-10} \text{ M}$ , respectively. Sensitive SERS detection of PAHs in actual soil environment was also proved. Furthermore, photocatalytic performance of  $\text{Fe}_3\text{O}_4/$

Cu<sub>2</sub>O-Ag NCs for degradation of PAHs was evaluated. Compared with Fe<sub>3</sub>O<sub>4</sub>/Cu<sub>2</sub>O NCs, Fe<sub>3</sub>O<sub>4</sub>/Cu<sub>2</sub>O-Ag NCs exhibited higher photocatalytic activity as a consequence of the formation of Schottky barrier at the Cu<sub>2</sub>O-Ag interface. Under visible light irradiation, Nap, BaP and Ant were almost completely degraded within 60, 140 and 180 min, respectively. Fe<sub>3</sub>O<sub>4</sub>/Cu<sub>2</sub>O-Ag NCs possessed superparamagnetic properties, and the Ms value was 41.2 emu·g<sup>-1</sup>, which endowed them with the ability to be recycled. This research not only provides a novel avenue for the SERS detection and visible light-driven photocatalytic degradation of PAHs, but also shows great potential in ensuring environmental safety to protect public health.

## CRediT authorship contribution statement

**Jie Huang:** Investigation, Methodology, Formal analysis, Writing – original draft. **Tianxiang Zhou:** Investigation. **Wenshi Zhao:** Formal analysis. **Sicheng Cui:** Conceptualization. **Rui Guo:** Data curation. **Dan Li:** Visualization. **Naveen Reddy Kadasala:** Validation. **Donglai Han:** Methodology. **Yuhong Jiang:** Funding acquisition. **Yang Liu:** Conceptualization, Funding acquisition, Writing – review & editing, Supervision. **Huilian Liu:** Supervision.

## Data availability

Data will be made available on request.

## Declaration of Competing Interest

The authors declare that they have no known competing financial interests or personal relationships that could have appeared to influence the work reported in this paper.

## Acknowledgements

This work was funded by the National Natural Science Foundation of China, China (Grant Numbers 21676115), Program for the development of Science and Technology of Jilin province, China (Grant Numbers 20200301043RQ and 20200201022JC), Program for Science and Technology of Education Department of Jilin Province, China (Grant Numbers JJKH20210611KJ and JJKH20220444KJ) and Open Program for Key Laboratory of Novel Materials for Sensor of Zhejiang Province of Hangzhou Dianzi University (Grant Numbers ZJKNMS2021006).

## Appendix A. Supplementary material

Supplementary data to this article can be found online at <https://doi.org/10.1016/j.jcis.2022.08.036>.

## References

- [1] R. Stading, G. Gastelum, C. Chu, W. Jiang, B. Moorthy, Molecular mechanisms of pulmonary carcinogenesis by polycyclic aromatic hydrocarbons (PAHs): Implications for human lung cancer, *Semin. Cancer Biol.* 76 (2021) 3–16.
- [2] Y. Liu, H. Hu, G. Zanaroli, P. Xu, H. Tang, A *Pseudomonas* sp. strain uniquely degrades PAHs and heterocyclic derivatives via lateral dioxygenation pathways, *J. Hazard. Mater.* 403 (2021) 123956.
- [3] A.J. Rascón, A. Azzouz, E. Ballesteros, Multiresidue determination of polycyclic aromatic hydrocarbons in edible oils by liquid-liquid extraction–solid-phase extraction–gas chromatography–mass spectrometry, *Food Control* 94 (2018) 268–275.
- [4] O. Idowu, M. Carbery, W. O'Connor, P. Thavamani, Speciation and source apportionment of polycyclic aromatic compounds (PACs) in sediments of the largest salt water lake of Australia, *Chemosphere* 246 (2020) 125779.
- [5] G. Fellet, F. Pošćić, S. Licen, L. Marchiol, R. Musetti, A. Tolloi, P. Barbieri, G. Zerbi, PAHs accumulation on leaves of six evergreen urban shrubs: a field experiment, *Atmos. Pollut. Res.* 7 (5) (2016) 915–924.
- [6] A. Ranjbar Jafarabadi, S. Mashjoo, A. Riyahi Bakhtiari, C. Jadot, Dietary intake of polycyclic aromatic hydrocarbons (PAHs) from coral reef fish in the Persian Gulf - Human health risk assessment, *Food Chem.* 329 (2020) 127035.
- [7] T. Zhang, H. Wu, B. Yan, Y. Zhang, C. Wei, Enhancement of PAHs biodegradation in biosurfactant/phenol system by increasing the bioavailability of PAHs, *Chemosphere* 266 (2021) 128941.
- [8] M. Kumar, N.S. Bolan, S.A. Hoang, A.D. Sawarkar, T. Jasemizad, B. Gao, S. Keerthanani, L.P. Padhye, L. Singh, S. Kumar, M. Vithanage, Y. Li, M. Zhang, M.B. Kirkham, A. Vinu, J. Rinklebe, Remediation of soils and sediments polluted with polycyclic aromatic hydrocarbons: To immobilize, mobilize, or degrade?, *J. Hazard. Mater.* 420 (2021) 126534.
- [9] A. Imam, S. Kumar Suman, P.K. Kanaujia, A. Ray, Biological machinery for polycyclic aromatic hydrocarbons degradation: A review, *Bioresour. Technol.* 343 (2022) 126121.
- [10] V. Sathish, M.M. Krishnan, M. Velayudham, P. Thanasekaran, K.-L. Lu, S. Rajagopal, Host-guest interaction studies of polycyclic aromatic hydrocarbons (PAHs) in alkoxy bridged binuclear rhenium (I) complexes, *Spectrochim. Acta A* 222 (2019) 117160.
- [11] C. Xu, Q. Liu, J. Liang, Z. Weng, J. Xu, Z. Jiang, A. Gu, Urinary biomarkers of polycyclic aromatic hydrocarbons and their associations with liver function in adolescents, *Environ. Pollut.* 278 (2021) 116842.
- [12] Y. Zhang, X. Chen, Y. Zhang, Analytical chemistry, formation, mitigation, and risk assessment of polycyclic aromatic hydrocarbons: From food processing to in vivo metabolic transformation, *Compr. Rev. Food Sci. F* 20 (2) (2021) 1422–1456.
- [13] J. Tang, S. Ma, R. Liu, C. Yue, G. Li, Y. Yu, Y. Yang, T. An, The pollution profiles and human exposure risks of chlorinated and brominated PAHs in indoor dusts from e-waste dismantling workshops: Comparison of GC-MS, GC-MS/MS and GC x GC-MS/MS determination methods, *J. Hazard. Mater.* 394 (2020) 122573.
- [14] Y. Huang, J. Wei, J. Song, M. Chen, Y. Luo, Determination of low levels of polycyclic aromatic hydrocarbons in soil by high performance liquid chromatography with tandem fluorescence and diode-array detectors, *Chemosphere* 92 (8) (2013) 1010–1016.
- [15] Z. Yu, M.F. Grasso, H.H. Sorensen, P. Zhang, Ratiometric SERS detection of polycyclic aromatic hydrocarbons assisted by beta-cyclodextrin-modified gold nanoparticles, *Microchim. Acta* 186 (6) (2019) 391.
- [16] A. Castro-Grijalba, V. Montes-García, M.J. Cordero-Ferradás, E. Coronado, J. Pérez-Juste, I. Pastoriza-Santos, SERS-based molecularly imprinted plasmonic sensor for highly sensitive PAH detection, *ACS Sens.* 5 (3) (2020) 693–702.
- [17] X. Gong, X. Liao, Y. Li, H. Cao, Y. Zhao, H. Li, D.P. Cassidy, Sensitive detection of polycyclic aromatic hydrocarbons with gold colloid coupled chloride ion SERS sensor, *Analyst* 144 (22) (2019) 6698–6705.
- [18] H. Hou, P. Wang, J. Zhang, C. Li, Y. Jin, Graphene oxide-supported Ag nanoplates as LSPR tunable and reproducible substrates for SERS applications with optimized sensitivity, *ACS Appl. Mater. Inter.* 7 (32) (2015) 18038–18045.
- [19] N.D. Jayram, D. Aishwarya, S. Sonia, D. Mangalaraj, P.S. Kumar, G.M. Rao, Analysis on superhydrophobic silver decorated copper oxide nanostructured thin films for SERS studies, *J. Colloid Interf. Sci.* 477 (2016) 209–219.
- [20] Y. Sang, X. Chen, L. Zhang, D. Li, H. Xu, Electrospun polymeric nanofiber decorated with sea urchin-like gold nanoparticles as an efficient and stable SERS platform, *J. Colloid Interf. Sci.* 590 (2021) 125–133.
- [21] Y. Long, H. Li, Z. Du, M. Geng, Z. Liu, Confined Gaussian-distributed electromagnetic field of tin(II) chloride-sensitized surface-enhanced Raman scattering (SERS) optical fiber probe: From localized surface plasmon resonance (LSPR) to waveguide propagation, *J. Colloid Interf. Sci.* 581 (Pt B) (2021) 698–708.
- [22] S.M. Morton, D.W. Silverstein, L. Jensen, Theoretical studies of plasmonics using electronic structure methods, *Chem. Rev.* 111 (6) (2011) 3962–3994.
- [23] Y. Li, Y. Wang, M. Wang, J. Zhang, Q. Wang, H. Li, A molecularly imprinted nanoprobe incorporating Cu<sub>2</sub>O@Ag nanoparticles with different morphologies for selective SERS based detection of chlorophenols, *Microchim. Acta* 187 (1) (2019) 59.
- [24] R. Su, Y. Quan, S. Yang, M. Hu, J. Yang, M. Gao, Destroying the symmetric structure to promote phase transition: Improving the SERS performance and catalytic activity of MoS<sub>2</sub> nanoflowers, *J. Alloy. Compd.* 886 (2021) 161268.
- [25] S. Wang, J. Cheng, C. Han, J. Xie, A Versatile SERS sensor for multiple determinations of polycyclic aromatic hydrocarbons and its application potential in analysis of fried foods, *Int. J. Anal. Chem.* 2020 (2020) 2428029.
- [26] N.R. Kadasala, A. Wei, Trace detection of tetrabromobisphenol A by SERS with DMAP-modified magnetic gold nanoclusters, *Nanoscale* 7 (25) (2015) 10931–10935.
- [27] X. Wang, Q. Xu, X. Hu, F. Han, C. Zhu, Silver-nanoparticles/graphene hybrids for effective enrichment and sensitive SERS detection of polycyclic aromatic hydrocarbons, *Spectrochim. Acta A* 228 (2020) 117783.
- [28] A. Chatterjee, D.J.G. Gale, D. Grebennikov, L.D. Whelan, E.F. Merschrod S., Surface potential and morphology mapping to investigate analyte adsorption effects on surface enhanced Raman scattering (SERS), *Chem. Commun.* 53(88) (2017) 12024–12027.
- [29] W. Li, C. Li, N. Zhu, H. Yuan, Y. Shen, The extent of sludge solubilization allows to estimate the efficacy of ozonation for removal of polycyclic aromatic hydrocarbons (PAHs) in municipal sewage sludge, *J. Hazard. Mater.* 413 (2021) 125404.
- [30] S. Huo, H. An, J. Yu, X. Mao, Z. Zhang, L. Bai, Y. Huang, P. Zhou, Pyrolytic in situ magnetization of metal-organic framework MIL-100 for magnetic solid-phase extraction, *J. Chromatogr. A* 1517 (2017) 18–25.

- [31] D. Huang, B. Xu, J. Wu, P.C. Brookes, J. Xu, Adsorption and desorption of phenanthrene by magnetic graphene nanomaterials from water: Roles of pH, heavy metal ions and natural organic matter, *Chem. Eng. J.* 368 (2019) 390–399.
- [32] G. Zhang, L. He, X. Guo, Z. Han, L. Ji, Q. He, L. Han, K. Sun, Mechanism of biochar as a biostimulation strategy to remove polycyclic aromatic hydrocarbons from heavily contaminated soil in a coking plant, *Geoderma* 375 (2020) 114497.
- [33] V.-H. Nguyen, L.-A. Phan Thi, Q. Van Le, P. Singh, P. Raizada, P. Kajitvichyanukul, Tailored photocatalysts and revealed reaction pathways for photodegradation of polycyclic aromatic hydrocarbons (PAHs) in water, soil and other sources, *Chemosphere* 260 (2020) 127529.
- [34] J. Kou, Z. Li, Y. Guo, J. Gao, M. Yang, Z. Zou, Photocatalytic degradation of polycyclic aromatic hydrocarbons in GaN:ZnO solid solution-assisted process: Direct hole oxidation mechanism, *J. Mol. Catal. A-Chem.* 325 (1–2) (2010) 48–54.
- [35] X. Sun, J. Bai, D. Dong, Z. Fan, UV Assisted Photocatalytic Remediation of Polycyclic Aromatic Hydrocarbons (PAHs) in Sewage Sludge Addition Soils Using Synthesized Nanometer Mixed-crystal  $\text{TiO}_2$ : Experiment and Simulation, *Soil Sediment Contam.* 31 (5) (2021) 572–585.
- [36] P. Zeng, Q. Zhang, X. Zhang, T. Peng, Graphite oxide- $\text{TiO}_2$  nanocomposite and its efficient visible-light-driven photocatalytic hydrogen production, *J. Alloy. Compd.* 516 (2012) 85–90.
- [37] Y. Jia, N. Shang, X. He, A. Nsabimana, Y. Gao, J. Ju, X. Yang, Y. Zhang, Electrocatalytically active cuprous oxide nanocubes anchored onto macroporous carbon composite for hydrazine detection, *J. Colloid Interf. Sci.* 606 (2) (2022) 1239–1248.
- [38] M. Shao, D. Liu, B. Yan, X. Feng, X. Zhang, Y. Zhang, Layer-by-Layer Electrodeposition of  $\text{FTO}/\text{TiO}_2/\text{Cu}_2\text{O}/\text{CeO}_2$  ( $1 < x < 2$ ) Photocatalysts with High Peroxidase-Like Activity by Greatly Enhanced Singlet Oxygen Generation, *Small Methods* 5 (7) (2021) 2100423.
- [39] T. Wu, H. Zheng, Y. Kou, X. Su, N.R. Kadasala, M. Gao, L. Chen, D. Han, Y. Liu, J. Yang, Self-sustainable and recyclable ternary  $\text{Au}/\text{Cu}_2\text{O}-\text{Ag}$  nanocomposites: application in ultrasensitive SERS detection and highly efficient photocatalysis of organic dyes under visible light, *Microsyst. Nanoeng.* 7 (2021) 23.
- [40] Z. Yang, C. Ma, W. Wang, M. Zhang, X. Hao, S. Chen, Fabrication of  $\text{Cu}_2\text{O}-\text{Ag}$  nanocomposites with enhanced durability and bactericidal activity, *J. Colloid Interf. Sci.* 557 (2019) 156–167.
- [41] G. Baffou, I. Bordenacchini, A. Baldi, R. Quidant, Simple experimental procedures to distinguish photothermal from hot-carrier processes in plasmonics, *Light-Sci. Appl.* 9 (2020) 108.
- [42] J.-Y. Jung, J.W. Hur, K. Kim, H.-S. Han, Evaluation of floc-harvesting technologies in biofloc technology (BFT) system for aquaculture, *Bioresour. Technol.* 314 (2020) 123719.
- [43] S.K.S. Patel, S.H. Choi, Y.C. Kang, J.-K. Lee, Eco-friendly composite of  $\text{Fe}_3\text{O}_4$ -reduced graphene oxide particles for efficient enzyme immobilization, *ACS Appl. Mater. Int.* 9 (3) (2017) 2213–2222.
- [44] A. Barzkar, A.S. Beni, In situ synthesis of  $\text{SO}_3\text{H}$  supported  $\text{Fe}_3\text{O}_4$ @resorcinol-formaldehyde resin core/shell and its catalytic evaluation towards the synthesis of hexahydroquinoline derivatives in green conditions, *RSC Adv.* 10 (68) (2020) 41703–41712.
- [45] C. Yuan, X. Wang, X. Yang, A.A. Alghamdi, F.A. Alharthi, X. Cheng, Y. Deng, Sulfonic acid-functionalized core-shell  $\text{Fe}_3\text{O}_4$ @carbon microspheres as magnetically recyclable solid acid catalysts, *Chinese Chem. Lett.* 32 (6) (2021) 2079–2085.
- [46] M. Nasrollahzadeh, M. Sajjadi, H.A. Khonakdar, Synthesis and characterization of novel  $\text{Cu}(\text{II})$  complex coated  $\text{Fe}_3\text{O}_4$ @ $\text{SiO}_2$  nanoparticles for catalytic performance, *J. Mol. Struct.* 1161 (2018) 453–463.
- [47] P.S. Pinto, G.D. Lanza, M.N. Souza, J.D. Ardisson, R.M. Lago, Surface restructuring of red mud to produce  $\text{FeOx}(\text{OH})_y$  sites and mesopores for the efficient complexation/adsorption of beta-lactam antibiotics, *Environ. Sci. Pollut. R.* 25 (7) (2018) 6762–6771.
- [48] Y. Liu, Y. Zhang, Q. Kou, Y. Chen, D. Han, D. Wang, Z. Lu, L. Chen, J. Yang, G. Xing, Eco-friendly seeded  $\text{Fe}_3\text{O}_4$ -Ag nanocrystals: a new type of highly efficient and low cost catalyst for methylene blue reduction, *RSC Adv.* 8 (4) (2018) 2209–2218.
- [49] Y. Chen, Y. Zhang, Q. Kou, Y. Liu, D. Han, D. Wang, Y. Sun, Y. Zhang, Y. Wang, Z. Lu, L. Chen, J. Yang, G. Xing, Enhanced catalytic reduction of 4-nitrophenol driven by  $\text{Fe}_3\text{O}_4$ -Au magnetic nanocomposite interface engineering: from facile preparation to recyclable application, *Nanomaterials-Basel* 8 (5) (2018) 353.
- [50] A. Herzog, A. Bergmann, H.S. Jeon, J. Timoshenko, S. Kuhl, C. Rettenmaier, M. Lopez Luna, F.T. Haase, B. Roldan Cuena, Operando investigation of Ag-decorated  $\text{Cu}_2\text{O}$  nanocube catalysts with enhanced  $\text{CO}_2$  electroreduction toward liquid products, *Angew. Chem. Int. Ed.* 60 (13) (2021) 7426–7435.
- [51] Q. Chen, C. Shi, L. Qin, S.-Z. Kang, X. Li, A low-cost 3D core-shell nanocomposite as ultrasensitive and stable surface enhanced Raman spectroscopy substrate, *Sens. Actuat. B-Chem.* 327 (2021) 128907.
- [52] Q.U. Ain, U. Rasheed, M. Yaseen, H. Zhang, Z. Tong, Superior dye degradation and adsorption capability of polydopamine modified  $\text{Fe}_3\text{O}_4$ -pillared bentonite composite, *J. Hazard. Mater.* 397 (2020) 122758.
- [53] T. Xu, R. Qu, Y. Zhang, C. Sun, Y. Wang, X. Kong, X. Geng, C. Ji, Preparation of bifunctional polysilsesquioxane/carbon nanotube magnetic composites and their adsorption properties for Au (III), *Chem. Eng. J.* 410 (2021) 128225.
- [54] M. Bae, H. Lee, K. Yoo, S. Kim, Copper(I) selective chemisorption on magnetite ( $\text{Fe}_3\text{O}_4$ ) over gold(I) ions in chloride solution with cyanide, *Hydrometallurgy* 201 (2021) 105560.
- [55] N. Wang, Y. Zhou, K. Chen, T. Wang, P. Sun, C. Wang, X. Chuai, S. Zhang, X. Liu, G. Lu, Double shell  $\text{Cu}_2\text{O}$  hollow microspheres as sensing material for high performance n-propanol sensor, *Sens. Actuat. B-Chem.* 333 (2021) 129540.
- [56] F. Zhang, Y. Li, M. Qi, Z. Tang, Y. Xu, Boosting the activity and stability of  $\text{Ag}-\text{Cu}_2\text{O}/\text{ZnO}$  nanorods for photocatalytic  $\text{CO}_2$  reduction, *Appl. Catal. B-Environ.* 268 (2020) 118380.
- [57] C. Ma, Z. Yang, W. Wang, M. Zhang, X. Hao, S. Zhu, S. Chen, Fabrication of  $\text{Ag}-\text{Cu}_2\text{O}/\text{PANI}$  nanocomposites for visible-light photocatalysis triggering super antibacterial activity, *J. Mater. Chem. C* 8 (8) (2020) 2888–2898.
- [58] Z. Zhang, R. Song, Z. Yu, W. Huang, Crystal-plane effect of  $\text{Cu}_2\text{O}$  templates on compositions, structures and catalytic performance of  $\text{Ag}/\text{Cu}_2\text{O}$  nanocomposites, *CrystEngComm* 21 (12) (2019) 2002–2008.
- [59] Y. Kou, T. Wu, H. Zheng, N.R. Kadasala, S. Yang, C. Guo, L. Chen, Y. Liu, J. Yang, Recyclable magnetic MIP-based SERS sensors for selective, sensitive, and reliable detection of paclobutrazol residues in complex environments, *ACS Sustain. Chem. Eng.* 8 (38) (2020) 14549–14556.
- [60] C. Yao, X. Gao, X. Liu, Y. Shen, A. Xie, In-situ preparation of Ferrero® chocolate-like  $\text{Cu}_2\text{O}@ \text{Ag}$  microsphere as SERS substrate for detection of thiram, *J. Mater. Res. Technol.* 11 (2021) 857–865.
- [61] S. Lin, H. Guan, Y. Liu, S. Huang, J. Li, W. Hasi, Y. Xu, J. Zou, B. Dong, Binary plasmonic assembly films with hotspot-type-dependent surface-enhanced Raman scattering properties, *ACS Appl. Mater. Inter.* 13 (44) (2021) 53289–53299.
- [62] Y. Wang, M. Zhang, H. Ma, H. Su, A. Li, W. Ruan, B. Zhao, Surface plasmon resonance from gallium-doped zinc oxide nanoparticles and their electromagnetic enhancement contribution to surface-enhanced Raman scattering, *ACS Appl. Mater. Inter.* 13 (29) (2021) 35038–35045.
- [63] Z. Zhu, B. Bai, O. You, Q. Li, S. Fan, Fano resonance boosted cascaded optical field enhancement in a plasmonic nanoparticle-in-cavity nanoantenna array and its SERS application, *Light-Sci. Appl.* 4 (6) (2015) e296–e.
- [64] J. Li, Y. Zhang, S. Ding, R. Pannesar, S. Tian, Core-shell nanoparticle-enhanced Raman spectroscopy, *Chem. Rev.* 117 (7) (2017) 5002–5069.
- [65] M.E. Koleva, N.N. Nedyalkov, R. Nikov, R. Nikov, G. Atanasova, D. Karashanova, V.I. Nuzhdin, V.F. Valeev, A.M. Rogov, A.L. Stepanov, Fabrication of  $\text{Ag}/\text{ZnO}$  nanostructures for SERS applications, *Appl. Surf. Sci.* 508 (2020) 145227.
- [66] X. Xiu, L. Hou, J. Yu, S. Jiang, C. Li, X. Zhao, Q. Peng, S. Qiu, C. Zhang, B. Man, Z. Li, Manipulating the surface-enhanced Raman spectroscopy (SERS) activity and plasmon-driven catalytic efficiency by the control of  $\text{Ag NP}/\text{graphene}$  layers under optical excitation, *Nanophotonics* 10 (5) (2021) 1529–1540.
- [67] A.E. Kandjani, M. Mohammadtaheeri, A. Thakkar, S.K. Bhargava, V. Bansal, Zinc oxide/silver nanoarrays as reusable SERS substrates with controllable 'hot-spots' for highly reproducible molecular sensing, *J. Colloid Interf. Sci.* 436 (2014) 251–257.
- [68] S. Yang, J. Yao, Y. Quan, M. Hu, R. Su, M. Gao, D. Han, J. Yang, Monitoring the charge-transfer process in a Nd-doped semiconductor based on photoluminescence and SERS technology, *Light-Sci. Appl.* 9 (2020) 117.
- [69] J.R. Lombardi, R.L. Birke, L.A. Sanchez, I. Bernard, S. Sun, The effect of molecular structure on voltage induced shifts of charge transfer excitation in surface enhanced Raman scattering, *Chinese Chem. Lett.* 104 (1984) 240–247.
- [70] L. Chen, F. Zhang, X. Deng, X. Xue, L. Wang, Y. Sun, J. Feng, Y. Zhang, Y. Wang, Y. M. Jung, SERS study of surface plasmon resonance induced carrier movement in  $\text{Au}/\text{Cu}_2\text{O}$  core-shell nanoparticles, *Spectrochim. Acta A* 189 (2018) 608–612.
- [71] Z. Yi, X. Xu, X. Kang, Y. Zhao, S. Zhang, W. Yao, Y. Yi, J. Luo, C. Wang, Y. Yi, Y. Tang, Fabrication of well-aligned  $\text{ZnO}@ \text{Ag}$  nanorod arrays with effective charge transfer for surface-enhanced Raman scattering, *Surf. Coat. Tech.* 324 (2017) 257–263.
- [72] X. Jiang, X. Sun, D. Yin, X. Li, M. Yang, X. Han, L. Yang, B. Zhao, Recyclable  $\text{Au}-\text{TiO}_2$  nanocomposite SERS-active substrates contributed by synergistic charge-transfer effect, *PCCP* 19 (18) (2017) 11212–11219.
- [73] J. Yang, M. Pan, K. Liu, X. Xie, S. Wang, L. Hong, S. Wang, Core-shell  $\text{AuNRs}@ \text{Ag}$ -enhanced and magnetic separation-assisted SERS immunosensing platform for amantadine detection in animal-derived foods, *Sens. Actuat. B-Chem.* 349 (2021) 130783.
- [74] C. Ye, Z. Zhu, X. Li, H. Zhou, M. Zhang, L. Yan, Z. Chen, Y. Huang, Y. Wu, ZIF-8 derived  $\text{TiO}_2/\text{ZnO}$  heterostructure decorated with  $\text{AgNPs}$  as SERS sensor for sensitive identification of trace pesticides, *J. Alloy. Compd.* 901 (2022) 163675.
- [75] D. Pan, J. Jiao, Z. Li, Y. Guo, C. Feng, Y. Liu, L. Wang, M. Wu, Efficient separation of electron-hole pairs in graphene quantum dots by  $\text{TiO}_2$  heterojunctions for dye degradation, *ACS Sustain. Chem. Eng.* 3 (10) (2015) 2405–2413.
- [76] E.J.C. Dias, R. Yu, F.J. Garcia de Abajo, Thermal manipulation of plasmons in atomically thin films, *Light-Sci. Appl.* 9 (2020) 87.
- [77] M. Svedendahl, R. Verre, M. Käll, Refractometric biosensing based on optical phase flips in sparse and short-range-ordered nanoplasmonic layers, *Light-Sci. Appl.* 3 (11) (2014) e220–e.
- [78] H. Qin, Q. Wei, J. Wu, F. Yang, B. Zhou, Y. Wang, S. Tian, Effects of  $\text{Ag}$  nanoparticles on the visible-light-driven photocatalytic properties of  $\text{Cu}_2\text{O}$  nanocubes, *Mater. Chem. Phys.* 232 (2019) 240–245.
- [79] A. Sabbah, I. Shown, M. Qorbani, F.-Y. Fu, T.-Y. Lin, H.-L. Wu, P.-W. Chung, C.-I. Wu, S.R.M. Santiago, J.-L. Shen, K.-H. Chen, L.-C. Chen, Boosting photocatalytic  $\text{CO}_2$  reduction in a  $\text{ZnS}/\text{ZnIn}_2\text{S}_4$  heterostructure through strain-induced direct Z-scheme and a mechanistic study of molecular  $\text{CO}_2$  interaction thereon, *Nano Energy* 93 (2022) 106809.
- [80] Y. Liu, J. Kong, J. Yuan, W. Zhao, X. Zhu, C. Sun, J. Xie, Enhanced photocatalytic activity over flower-like sphere  $\text{Ag}/\text{Ag}_2\text{CO}_3/\text{BiVO}_4$  plasmonic heterojunction photocatalyst for tetracycline degradation, *Chem. Eng. J.* 331 (2018) 242–254.



- [81] T. Wu, H. Zheng, Y. Kou, S. Jin, Y. Jiang, M. Gao, L. Chen, N.R. Kadasala, Y. Liu, Rhombic dodecahedral  $\text{Cu}_2\text{O}/\text{Ag}$ -3D  $\text{Fe}_3\text{O}_4$  micro-flower composites for water purification under visible light irradiation, *J. Alloy. Compd.* 858 (2021) 157698.
- [82] Y. Deng, L. Tang, G. Zeng, C. Feng, H. Dong, J. Wang, H. Feng, Y. Liu, Y. Zhou, Y. Pang, Plasmonic resonance excited dual Z-scheme  $\text{BiVO}_4/\text{Ag}/\text{Cu}_2\text{O}$  nanocomposite: synthesis and mechanism for enhanced photocatalytic performance in recalcitrant antibiotic degradation, *Environ Sci-Nano* 4 (7) (2017) 1494–1511.
- [83] L. Jian, D. Cai, G. Su, D. Lin, M. Lin, J. Li, J. Liu, X. Wan, S. Tie, S. Lan, The accelerating effect of silver ion on the degradation of methyl orange in  $\text{Cu}_2\text{O}$  system, *Appl. Catal. A-Gen.* 512 (2016) 74–84.
- [84] P. Qiu, J. Xiong, M. Lu, L. Liu, W. Li, Z. Wen, W. Li, R. Chen, G. Cheng, Integrated p-n/Schottky junctions for efficient photocatalytic hydrogen evolution upon  $\text{Cu}/\text{TiO}_2\text{-Cu}_2\text{O}$  ternary hybrids with steering charge transfer, *J. Colloid Interf. Sci.* 622 (2022) 924–937.
- [85] H. Feng, W. Wang, W. Wang, M. Zhang, C. Wang, C. Ma, W. Li, S. Chen, Charge transfer channels of silver @ cuprous oxide heterostructure core-shell nanoparticles strengthen high photocatalytic antibacterial activity, *J. Colloid Interf. Sci.* 601 (2021) 531–543.
- [86] A. Errokh, W. Cheikhrouhou, A.M. Ferrara, A.M. Botelho do Rego, S. Boufi, Cotton decorated with  $\text{Cu}_2\text{O}$ -Ag and  $\text{Cu}_2\text{O}$ -Ag-AgBr NPs via an in-situ sacrificial template approach and their antibacterial efficiency, *Colloid Surface B* 200 (2021) 111600.
- [87] C.E. Harvey, B.M. Weckhuysen, Surface- and Tip-Enhanced Raman spectroscopy as operando probes for monitoring and understanding heterogeneous catalysis, *Catal. Lett.* 145 (1) (2015) 40–57.
- [88] H.-K. Choi, W.-H. Park, C.-G. PARK, H.-H. Shin, K.S. Lee, Z.H. Kim, Metal-catalyzed chemical reaction of single molecules directly probed by vibrational spectroscopy, *J Am Chem Soc* 138(13) (2016) 4673–4684.
- [89] J. Miao, H. Yang, D. Zhu, A. Xie, F. Huang, S. Li, Y. Shen, A facile strategy for the preparation of a porous flower-like  $\text{Fe}_3\text{O}_4/\text{Cu}_2\text{O}/\text{Ag}$  nanocomposite with unexpected and recyclable photocatalytic activity under visible light irradiation, *Mater. Lett.* 163 (2016) 106–110.